Dispersion-cancelled imaging with chirped laser pulses

by

Michael Mazurek

A thesis
presented to the University of Waterloo
in fulfillment of the
thesis requirement for the degree of
Master of Science
in
Physics

Waterloo, Ontario, Canada, 2013

I hereby declare that I am the sole author of this thesis, except where noted. This is a true copy of the thesis, including any required final revisions, as accepted by my examiners.

I understand that my thesis may be made electronically available to the public.

Abstract

This thesis deals with chirped-pulse interferometry, an interferometric imaging technique with a resolution which is unaffected by the normally detrimental effects of sample dispersion. The thesis begins with some important background definitions and concepts. The properties of ultrafast laser pulses are discussed, and the nonlinear process of sum-frequency generation is defined. Three different interferometric imaging systems introduced, namely optical coherence tomography, quantum optical coherence tomography, and chirped-pulse interferometry. Understanding the first two techniques is key to realizing the benefits provided by the third.

In the first experiment a chirped-pulse interferometer is used to image the cells of an onion. This is the first time that a dispersion-cancelled technique has been used to image the interior structure of a biological sample. Laser pulses centred on 810 nm with 90 nm full-width at half-maximum bandwidth are chirped with a spatial light modulator in a 4f-system to create a superposition of frequency-anticorrelated pulses. The chirped pulses are sent into a Michelson interferometer with a sample of onion in one arm. The cellular structure of the onion is imaged to a depth of 0.5 mm with a resolution of $3.2 \pm 0.6\,\mu$m. The introduction of $132\,\text{fs}^2$ of quadratic dispersion in front of the sample does not affect the resolution of the image. A three-dimensional image of the sample's internal structure is created.

The second experiment uses a nonlinear chirping function to produce a narrower interference signal in a chirped-pulse interferometer than that given by linearly-chirped pulses; this competes with the inherently narrower signal seen in quantum optical coherence tomography systems. The nonlinear chirping function theoretically narrows the interference signal by 30%, matching the width of the quantum signal. Experimentally, a narrowing of 17% was observed. The nonlinear chirping function was shown to cancel the $132\,\text{fs}^2$ of unbalanced quadratic dispersion as effectively as the linear function.

One of the main sources of background noise in a chirped-pulse interferometer is a narrow-band component of sum-frequency generated light from the interferometer's intense reference beam. This background is at the same frequency and has the same bandwidth

as the signal. A third experiment is proposed in which the light in the sample and reference arms of the interferometer is chirped independently. If the light in both arms is a superposition of frequency-anticorrelated pulses with different average frequencies the interferometer should still be dispersion-cancelling, but the narrowband background will shift spectrally from the signal.

Acknowledgements

I first thank Kevin Resch who has been a great supervisor. He is always available and willing to discuss research, and I am looking forward to working with him while I pursue my Ph.D. I thank the other two members of my advisory committee, Dida Bizheva and Jonathan Baugh. I especially thank Dida for sharing her knowledge of optical coherence tomography and always offering her help. I also thank Matteo Mariantoni for agreeing to be on my examining committee.

All of the members of my research group have helped me over the last two years. Robert Prevedel assisted me the most when I first started in the group. He passed on a wealth of information in my first few months and he was always willing to answer my many questions about stuff in the lab. Kurt Schreiter was always willing to talk about the experiment, and his knowledge of LabVIEW came in handy more than once. Jonathan Lavoie gave me countless tips on alignment techniques, and he knows how to find absolutely anything in the lab. I had many useful discussions about chirped pulses with both Jon Lavoie and John Donohue. I thank all members of my group, including Deny Hamel, Kent Fisher, Megan Agnew, Lydia Vermeyden and Krister Shalm for always being available to bounce ideas off of.

I thank the Ontario Centres of Excellence, Canadian Foundation for Innovation, QuantumWorks, Industry Canada, and the Ontario Ministry of Research and Innovation for funding the experiments in this thesis. I also personally thank the National Science and Engineering Council of Canada, which funded me during my Master's.

Finally I thank my family, including my parents Cheryl and Dave and my sister Liz for their love and support.

Table of Contents

List of Tables

List of Figures

Chapter 1

Background

1.1 Low-coherence laser pulses

The experiments in this thesis used a pulsed titanium:sapphire laser which produced broadband laser pulses centred around 800 nm. Broadband laser pulses have short coherence times, and hence they are useful for interferometric imaging techniques as they can produce narrow interference signals. In the following section some important properties of low-coherence laser pulses are defined, and techniques to modify their length and shape are discussed.

1.1.1 Mathematical description of electric field

The electric field is described in the time domain by a real function $E(t)$. The field also has a complex representation in the frequency domain, $E(\omega)$, given by the Fourier transform of the time-dependent function [6]:

$$E(\omega) = \mathcal{F}\left(E\left(t\right)\right) = \int_{-\infty}^{\infty} dt\, E(t) e^{-i\omega t} = \left|E(\omega)\right| e^{i\phi(\omega)} \tag{1.1}$$

The inverse transform can be performed to obtain $E(t)$ from $E(\omega)$:

$$E(t) = \frac{1}{2\pi} \int_{-\infty}^{\infty} d\omega \, E(\omega) e^{i\omega t} \tag{1.2}$$

For convenience, the electric field can be split into two components, $E^+(\omega)$ and $E^-(\omega)$, corresponding to positive and negative frequencies, respectively:

$$E^{\pm}(\omega) = \begin{cases} E(\omega) & \text{for} \quad \pm\,\omega \geq 0 \\ 0 & \text{for} \quad \pm\,\omega < 0 \end{cases} \tag{1.3}$$

In the time domain, the electric field can then be written as a sum of two complex terms such that $E(t) = E^+(t) + E^-(t)$ where

$$E^+(t) = \frac{1}{2\pi} \int_{0}^{\infty} d\omega \, E^+(\omega) e^{i\omega t} \tag{1.4}$$

$$E^-(t) = \frac{1}{2\pi} \int_{-\infty}^{0} d\omega \, E^-(\omega) e^{i\omega t} \tag{1.5}$$

The positive part of the complex electric field, $E^+(t)$, can be written as a real amplitude multiplied by a complex phase:

$$E^+(t) = \frac{1}{2} \mathcal{E}(t) e^{i\psi(t)} e^{i\omega_l t} \tag{1.6}$$

The *carrier frequency* of the pulse is ω_l, and it is chosen to minimize the variation of the nonlinear phase term $\psi(t)$. It can be shown [6] that the pulse has an instantaneous frequency, $\omega(t)$, defined as

$$\omega(t) = \omega_l + \frac{d}{dt}\psi(t) \tag{1.7}$$

1.1.2 Pulse propagation through dispersive media

As a pulse propagates through an optical medium of length L it acquires a frequency-dependent phase $k(\omega)L$, and the output field can be related to the input as

$$E_{out}(\omega) = e^{-ik(\omega)L} E_{in}(\omega) \tag{1.8}$$

where the material's wavevector, $k(\omega)$, is given by

$$k(\omega) = \frac{\omega n(\omega)}{c} \tag{1.9}$$

The material's index of refraction is $n(\omega)$ and c is the speed of light in vacuum. The wavevector can be Taylor-expanded about the pulse carrier frequency ω_l:

$$k(\omega) = \sum_{n=0}^{\infty} b_n (\omega - \omega_l)^n \tag{1.10}$$

The coefficients b_n are given by

$$b_n = \frac{1}{n!} \frac{d^n}{d\omega^n} \phi(\omega) \Big|_{\omega=\omega_l} \tag{1.11}$$

The $n = 0$ term adds a constant phase and does not otherwise affect the pulse. The constant b_1 is called the group-delay dispersion (GDD) and it adds a constant delay to the pulse in the time domain. The b_2 term is called the group-velocity dispersion (GVD) and it adds a time-delay which is linearly dependent on frequency. This has the effect of either stretching or compressing the pulse in the time-domain but otherwise maintaining the shape of the amplitude envelope $E(t)$. The higher-order terms also add frequency-dependent delays and can change the shape of the envelope.

As an example, consider a pulse with a Gaussian electric field envelope, described by

$$E^+(\omega) = \begin{cases} e^{-\frac{(\omega-\omega_0)^2}{4\sigma^2}} & \text{for} \quad \omega \geq 0 \\ 0 & \text{for} \quad \omega < 0 \end{cases} \tag{1.12}$$

The pulse's spectral intensity, $I(\omega)$, is the squared-magnitude of the spectral amplitude, $|E(\omega)|^2$. Hence $I(\omega) = e^{-\frac{(\omega-\omega_0)^2}{2\sigma^2}}$. The pulse's *spectral bandwidth* is defined as the root-mean-square width of the spectral intensity, σ. The pulse is now propagated through an optical medium of length L and wavevector $k(\omega) = k_0 + \alpha(\omega - \omega_0) + \beta(\omega - \omega_0)^2$. The complex electric field of the pulse sent into to the medium is given by

$$E^+_{in}(t) = \frac{1}{2\pi}\int_0^\infty d\omega\, E^+(\omega)e^{i\omega t} \tag{1.13}$$

$$\approx \frac{1}{2\pi}\int_{-\infty}^\infty d\omega\, e^{-\frac{(\omega-\omega_0)^2}{4\sigma^2}}e^{i\omega t} \tag{1.14}$$

$$= \sqrt{\frac{\sigma^2}{\pi}}e^{-t^2\sigma^2}e^{i\omega_0 t} \tag{1.15}$$

where the approximation in the second step can be made if the pulse center frequency ω_0 is sufficiently greater than σ, such that the $e^{-\frac{(\omega-\omega_0)^2}{4\sigma^2}} \approx 0$ when $\omega < 0$. The input field has a carrier frequency ω_0, and a length in time proportional to σ^{-1}. The output field is given by

$$E^+_{out}(t) \approx \frac{1}{2\pi}\int_{-\infty}^\infty d\omega\, e^{-\frac{(\omega-\omega_0)^2}{4\sigma^2}}e^{-ik(\omega)L}e^{i\omega t} \tag{1.16}$$

$$= \sqrt{\frac{\sigma^2}{\pi(4i\beta\sigma^2+1)}}e^{-\frac{(t-\alpha L)^2\sigma^2}{1+(4\beta L\sigma^2)^2}}e^{i\frac{4(t-\alpha L)^2\beta L\sigma^4}{1+(4\beta L\sigma^2)^2}}e^{i(\omega_0 t - k_0 L)} \tag{1.17}$$

The group-delay term has delayed the output field by a time αL, and the GVD term has stretched the pulse in time by a factor $\sqrt{1+(4\beta L\sigma^2)^2}$. Note that the sign of β does not affect the length of the output pulse. The input pulse is *transform limited* since its length in time is the shortest it can be, given its spectral bandwidth. The carrier frequency is still ω_0, but the pulse now has a time-dependent instantaneous frequency given by differentiating the complex-phase terms of (1.17):

$$\omega(t) = \omega_0 + (t - \alpha L)\frac{8\beta L\sigma^4}{1+(4\beta L\sigma^2)^2} \tag{1.18}$$

The instantaneous frequency increases linearly in time; this is called a *chirped* pulse (Fig-

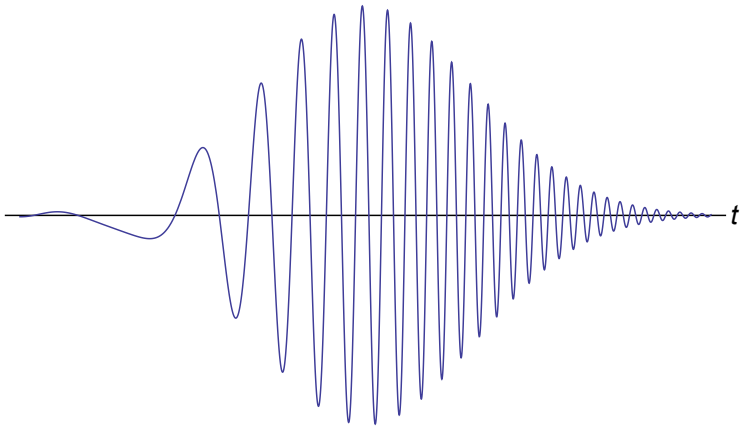

Figure 1.1: Electric field of a chirped laser pulse. The pulse has been chirped with positive GVD, and the instantaneous frequency of the pulse increases linearly with time.

ure 1.1). If the quadratic dispersion term is large enough to stretch the input pulse to many times its transform-limited length, (i.e., if $\beta L \gg 1/\sigma^2$), the instantaneous frequency can be simplified to

$$\omega(t) \approx \omega_0 + \frac{t - \alpha L}{2\beta L} \tag{1.19}$$

1.1.3 Interference and coherence length

Consider the interferometer in Figure 1.2. The input pulse in mode 1 has a positive-frequency electric field component of $E_1^+(\omega) \approx e^{-\frac{(\omega-\omega_0)^2}{4\sigma^2}} e^{i\phi(\omega)}$, where the approximation is necessary because the right-hand side of the expression includes negative frequencies, while the left-hand side does not. The pulse has a spectral bandwidth of ω, and an undetermined complex phase $\phi(\omega)$.

The pulse is split on a 50:50 beamsplitter and the light reflected into mode 2 acquires a phase $e^{i\pi} = -1$. The light in both arms is reflected from a mirror and returns to the beamsplitter. The light in mode 3 acquires an extra time delay τ, represented by the phase $e^{i\omega\tau}$. Modes 2 and 3 are combined on the beamsplitter, and the light in mode 3 acquires a

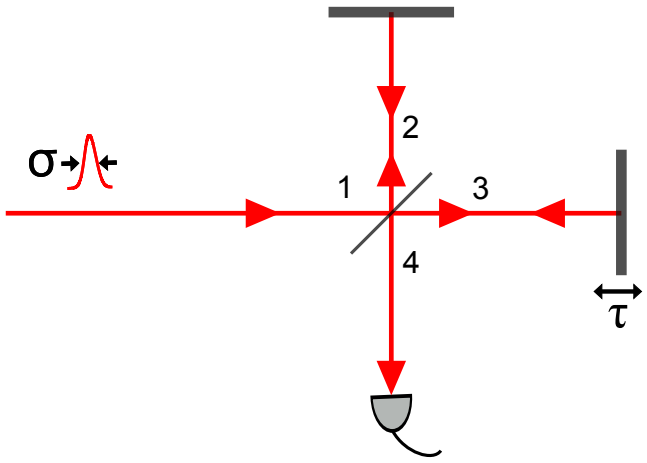

Figure 1.2: Interferometer for measuring coherence time. An pulse with bandwidth σ is incident on a 50:50 beamsplitter and each half of the split pulse travels in one arm of a Michelson interferometer. One arm of the interferometer contains a moveable mirror which is used to unbalance the path lengths of the interferometer by a distance $c\tau$. The intensity of light exiting the interferometer is measured as a function of the delay time, τ.

phase $e^{i\pi}$ from the reflection. The field in mode 4 is the sum of these fields, given by

$$E_4(\omega) = \frac{1}{\sqrt{2}} E_2(\omega) - \frac{1}{\sqrt{2}} E_3(\omega) = -\frac{1}{2} E_1(\omega) \left(1 + e^{i\omega\tau}\right) \tag{1.20}$$

The measured intensity in mode 4 is the squared-magnitude of the field, $|E_4(\omega)|^2$, integrated over all frequencies [6]:

$$I_4(\tau) = \frac{1}{2} \int d\omega \, e^{-\frac{(\omega-\omega_0)^2}{2\sigma^2}} \left(1 + \cos\omega\tau\right) \tag{1.21}$$

$$= \sqrt{2\pi\sigma^2} \left(1 + e^{-\frac{\tau^2\sigma^2}{2}} \cos\omega_0\tau\right) \tag{1.22}$$

The interference signal has a constant-background term and a cosine-modulated interference term. The gaussian envelope of the interference term has an RMS width of $\sigma_\tau = 1/\sigma$. This width is the *coherence time* of the pulse. To obtain an interference signal narrower than σ_τ, light with a broader bandwidth must be used. Note that the phase on the input

pulse, $\phi(\omega)$, is not present in the expression for the interference signal. Hence, changing the shape of the input pulse in the time-domain does not affect the coherence time of the pulse.

1.1.4 Custom pulse-shaping

One way to change the temporal profile of a laser pulse is to send it through a dispersive material, although this does not give one very much control over the pulse shape. It may be desirable to have the ability to add an arbitrary phase $\phi(\omega)$ to a pulse, and one way of doing so is to use a spatial light modulator (SLM) in a 4f set-up [16, 26, 32] as depicted in Figure 1.3. A pulse impinges on a grating, and the individual frequency components of the pulse are diffracted [6]. If the pulse is incident on the grating at an angle β from normal incidence, the frequency component ω' will be diffracted at an angle β', given by

$$\sin\beta' - \sin\beta = \frac{2\pi c}{\omega' d} = \frac{\lambda'}{d} \tag{1.23}$$

where d is the spacing between grooves in the grating and λ' is the wavelength corresponding to frequency ω'. After being diffracted the pulse is deflected from a prism mirror to a curved mirror with focal length f. The distance along the optic axis from the grating to the mirror is a distance f, so the mirror collimates the beam. The light travels a distance $2f$ to a second curved mirror where it is focused down to a second grating which recombines the light into a single spatial mode. The SLM is a one-dimensional array of liquid crystals with refractive indices which are controlled by an applied voltage across each crystal. Each crystal is independently controlled and can apply a phase between 0 and 2π to light passing through it. The SLM is positioned halfway between the two mirrors and hence each crystal applies a phase only to the narrow range of frequencies passing through it. With this system an arbitrary phase $\phi(\omega)$ can be applied to the pulse.

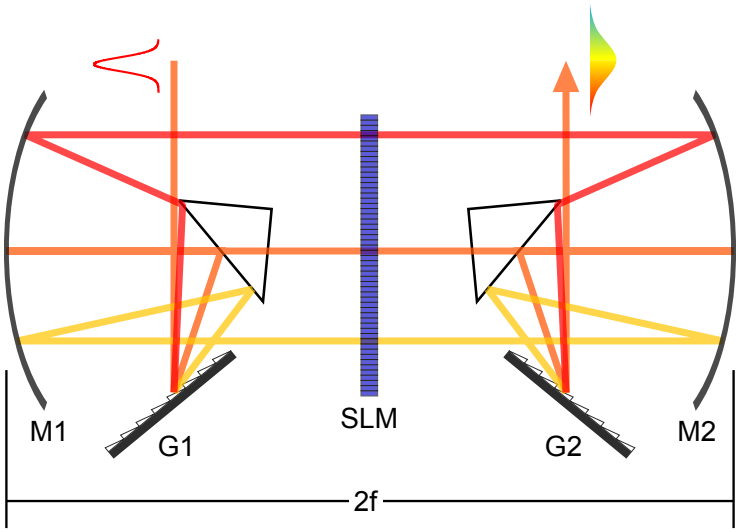

Figure 1.3: 4f system with SLM for applying a custom frequency dependent phase to a laser pulse. The input pulse is diffracted at grating G1 and, after being redirected with a prism mirror, is collimated by mirror M1 with focal length f. The collimated beam passes through an SLM then hits M2 which is a distance $2f$ from M1. The pulse is focused down onto G2 where all frequencies are recombined into a single spatial mode. Each liquid crystal in the SLM is independently controlled and applies a phase shift between 0 and 2π to the light passing through it, hence an arbitrary phase $\phi(\omega)$ can be applied to the pulse.

1.2 Second-order nonlinear materials

When an electric field $E(t)$ interacts with a material it induces a polarization $P(t)$ in the material [4]. Making the assumptions that the material is lossless, dispersionless, and responds instantaneously to the electric field, the polarization can be represented by

$$P(t) = \chi^{(1)}E(t) + \chi^{(2)}E^2(t) + \chi^{(3)}E^3(t) + \dots \tag{1.24}$$

where $\chi^{(1)}$ is a constant known as the *linear susceptibility*, and $\chi^{(n)}$ are n-th-rank tensors called the *n-th-order nonlinear optical susceptibilities* when $n > 1$. The $\chi^{(n)}$ terms are material-dependent and they relate the strength of the material's response to the n-th-order terms of the electric field. These terms are represented as scalars in this discussion, for simplicity. The electric field of two monochromatic plane waves of frequencies ω_1 and ω_2 is given by [4]

$$E(t) = E_1 e^{-i\omega_1 t} + E_2 e^{-i\omega_1 t} + c.c. \tag{1.25}$$

where E_1 and E_2 are the amplitudes of the waves. A field of this form will induce a second-order polarization of

$$P^{(2)}(t) = \chi^{(2)}E^2(t) \tag{1.26}$$

$$\begin{aligned} &= \chi^{(2)}[E_1^2 e^{-2i\omega_1 t} + E_2^2 e^{-2i\omega_2 t} + 2E_1E_2e^{-i(\omega_1+\omega_2)t} \\ &\quad + 2E_1E_2^* e^{-i(\omega_1-\omega_2)t} + c.c.] + 2\chi^{(2)}\left[E_1E_1^* + E_2E_2^*\right] \end{aligned} \tag{1.27}$$

The first two terms oscillate with frequencies $2\omega_1$ and $2\omega_2$, and these describe a process known as *second-harmonic generation*, in which light is created at these doubled frequencies. The second two terms oscillate with frequencies $\omega_1 + \omega_2$ and $\omega_1 - \omega_2$, and these are related to the processes *sum-frequency generation* (SFG) and *difference-frequency generation.*

Here we will focus on SFG. Each of the waves ω_1, ω_2, and $\omega_3 = \omega_1 + \omega_2$ will have a momentum wavevector in the nonlinear material $k_i = n_i\omega_i/c$ where n_i is the material's

refractive index at the i-th frequency. The wavevector mismatch, Δk is defined as

$$\Delta k = k_1 + k_2 - k_3 \tag{1.28}$$

It can be shown [4] that the intensity of SFG light at the frequency $\omega_3 = \omega_1 + \omega_2$ is given by

$$I_{\omega_3} = AL^2 \text{sinc}^2\left(\frac{\Delta kL}{2}\right) \tag{1.29}$$

where A is a constant proportional to the intensities of the input fields E_1 and E_2 as well as the strength of the second-order nonlinearity, $\chi^{(2)}$. L is called the *interaction length*; it is the length over which the two fields overlap inside the nonlinear crystal. For small values of L the intensity of the field increases quadratically with L. However, the efficiency of the SFG process quickly drops to zero as ΔkL becomes large.

1.2.1 Phase-matching

For better SFG efficiencies it is desirable for Δk to be small so the input fields can interact over a longer region L. The above discussion can be generalized to describe SFG with noncollinear input beams in birefringent nonlinear materials [4]. A birefringent material has a refractive index that is dependent on the polarization of the electric field. A birefringent *uniaxial* material is defined by an optic axis; light with *ordinary* polarization is polarized perpendicularly to the plane created by the propagation vector $\vec{k}$ and the optic axis, and light with polarization in this plane is said to have *extraordinary* polarization. A uniaxial material and exhibits refractive indices n_o and n_e for light that is polarized in the ordinary and extraordinary directions, respectively.

Figure 1.4 depicts an SFG set-up with noncollinear fields in a negative uniaxial crystal (where $n_e < n_o$). The two input fields have ordinary polarization, and the noncollinear angle between their propagation directions is 2ψ. The output field has extraordinary polarization, and propagates in the $\hat{z}$-direction. The electric field with frequency ω_i has wavevector $\vec{k}_i$, and, for small noncollinear angles, the wavevector mismatch can be approximated by the mismatch in the $\hat{z}$-direction. The condition for perfect phase-matching is

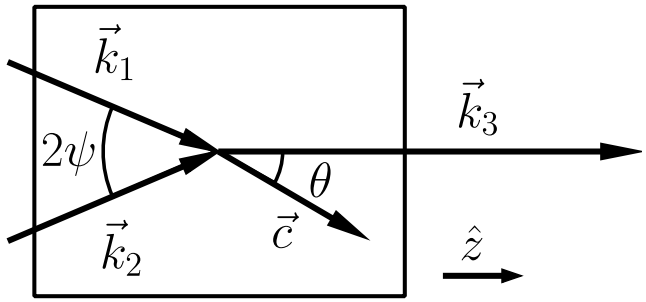

Figure 1.4: Sum-frequency generation with noncollinear input fields in a uniaxial nonlinear crystal. Two fields with wavevectors $\vec{k}_1$ and $\vec{k}_2$ enter a nonlinear material with noncollinear angle 2ψ between them. The material has an optic axis $\vec{c}$, an angle θ from the wavevector of the upconverted light, $\vec{k}_3$.

then

$$n_3^e \omega_3 = (n_1^o \omega_1 + n_2^o \omega_2) \cos\psi \tag{1.30}$$

If the angle between the material's optic axis and a field's propagation vector $\vec{k}$ is θ, the refractive index for the extraordinary polarization will be [4]

$$\frac{1}{n_e(\theta)^2} = \frac{\sin^2(\theta)}{\bar{n}_e^2} + \frac{\cos^2\theta}{n_o^2} \tag{1.31}$$

The parameter $\bar{n}_e$ is the principal extraordinary index, which is the value of n_e when $\theta = \pi/2$. Substituting (1.31) into (1.30) gives

$$n_3^e(\theta)\omega_3 = (n_1^o \omega_1 + n_2^o \omega_2) \cos\psi \tag{1.32}$$

which can be rearranged to give

$$\sin^2\theta = \frac{\frac{1}{(n_o(\omega_1)\omega_1 + n_o(\omega_2)\omega_2)^2 \cos^2\psi} - \frac{1}{n_o^2(\omega_3)\omega_3^2}}{\frac{1}{\omega_3^2}\left(\frac{1}{\bar{n}_e^2(\omega_3)} - \frac{1}{n_o^2(\omega_3)}\right)} \tag{1.33}$$

Hence the wavevector mismatch can be minimized by tuning the crystal angle θ and the noncollinear angle Ψ.

1.3 Optical coherence tomography

Optical coherence tomography (OCT) is an interferometric imaging technique which can be used to reconstruct the three-dimensional interior structure of a sample [9, 23, 31, 33]. A basic OCT set-up is shown in Figure 1.5. Light of bandwidth σ enters a Michelson interferometer which contains a sample in one arm (mode 1) and a moveable delay mirror in the other (mode 3). Light enters the sample and is reflected from different layers within the sample. The light from both interferometer arms is recombined on the beamsplitter, and the intensity of light in mode 3 is measured as a function of the delay τ in the reference arm. An interference pattern will be measured when the interferometer path lengths are balanced to within the coherence length of the source light, $1/\sigma$. For a sample with multiple internal reflecting interfaces, interference patterns will be observed at many values of τ corresponding to the positions of these interfaces. If the sample is moved laterally on a stage, many adjacent axial depth scans can be performed, and the results stitched together to form a two- or three-dimensional image of the internal sample structure.

Assuming that the light source has a gaussian frequency spectrum, the incoming electric field can be expressed in the frequency domain as $E(\omega) = \mathcal{E}e^{-(\omega-\omega_0)^2/4\sigma^2}$, where ω_0 is the center frequency, σ is the pulse bandwidth, and $\mathcal{E}$ is a complex amplitude. The light in mode 1 reflects from a layer a distance L below the sample surface, and the light in mode 2 reflects from the mirror which adds a delay τ. The sample has a wavevector of light $k(\omega)$ which can be expanded about the center frequency ω_0 to give $k(\omega) \approx k_0 + \alpha(\omega - \omega_0) + \beta(\omega - \omega_0)^2$. The phase acquired in mode 1 is represented by $\phi_1(\omega) = 2k(\omega)L$ and $\phi_2(\omega, \tau) = \omega\tau$ is the phase on the light in mode 2. The field in mode 3 is the sum of the fields in modes 1 and 2, $E_3(\omega, \tau) = E(\omega)e^{i\phi_1(\omega)} + E(\omega)e^{i\phi_2(\omega,\tau)}$, and the measured signal, $I(\tau)$, is the intensity in mode 3 given by:

$$I(\tau) = \int d\omega \, |E_3(\omega, \tau)|^2 \tag{1.34}$$

$$= \frac{1}{2} |\mathcal{E}|^2 \int d\omega e^{-\frac{(\omega-\omega_0)^2}{2\sigma^2}} \left|1 + \cos\left(2L(k_0 - \alpha\omega) + (2L\alpha - \tau)\omega + 2L\beta(\omega - \omega_0)^2\right)\right| \tag{1.35}$$

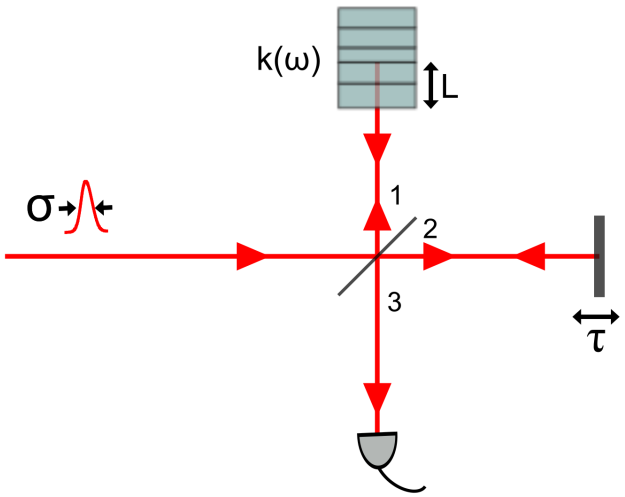

Figure 1.5: A white-light interferometer for optical coherence tomography. A laser with bandwidth σ is incident on a 50:50 beamsplitter. Half of the light reflects from a depth L inside a sample with wavevector $k(\omega)$, and the other half is delayed in the reference arm by a time τ. The light is recombined on the beamsplitter, and the signal is measured with a square-law detector. An interference pattern will be measured when the path lengths of the interferometer arms are balanced to within the coherence time of the light, $1/\sigma$.

Evaluating this signal gives an interference pattern which has an envelope proportional to the following gaussian function:

$$\exp\left[-\frac{\tau^2}{2}\frac{\sigma^2}{\sqrt{1+\epsilon^2\sigma^4}}\right] \tag{1.36}$$

where the simplification $\epsilon = 2L\beta$ has been used.

The signal's width is a minimum when no unbalanced second-order dispersion is present, and it has a value of $\Delta\tau_{\text{signal}} = 1/\sigma$. To increase the resolution of a white-light interferometer, a higher-bandwidth source can be used. However, in the high-dispersion limit where $\epsilon^2\sigma^4 \gg 1$, the signal width is $\Delta\tau_{\text{signal}} = \epsilon\sigma^2$. Hence using a higher-bandwidth source will amplify the negative effects of the second-order dispersion, which can have the undesirable effect of decreasing the interferometer resolution.

1.3.1 Quantum optical coherence tomography

Quantum optical coherence tomography (QOCT) is an interferometric imaging technique [1, 19, 20] which produces a signal with a width inversely proportional to the bandwidth of the interfered light, but which is insensitive to the presence of unbalanced quadratic dispersion in the interferometer [27, 28]. QOCT uses a Hong-Ou-Mandel (HOM) interferometer [12], which interferes pairs of frequency-entangled photons; the two photons in each pair travel through different arms of the interferometer, where they are recombined on a beamsplitter. If the two photons arrive at the beamsplitter at different times, they will each be independently reflected or transmitted with probability 1/2. If they arrive at the same time, however, they will interfere and "bunch", meaning that they will both exit from the same beamsplitter mode [12]. The QOCT signal is measured by placing single photon detectors in each output of the beamsplitter and recording the number of detection *coincidences* as a function of the time delay. This produces a dip when the interferometer path lengths are balanced.

Figure 1.6 depicts a HOM interferometer. The photon pairs are produced by spontaneous parametric down-conversion (SPDC), a process in which a single (pump) photon of frequency ω_3 is split into two lower-energy photons with frequencies ω_1 and ω_2. Due to

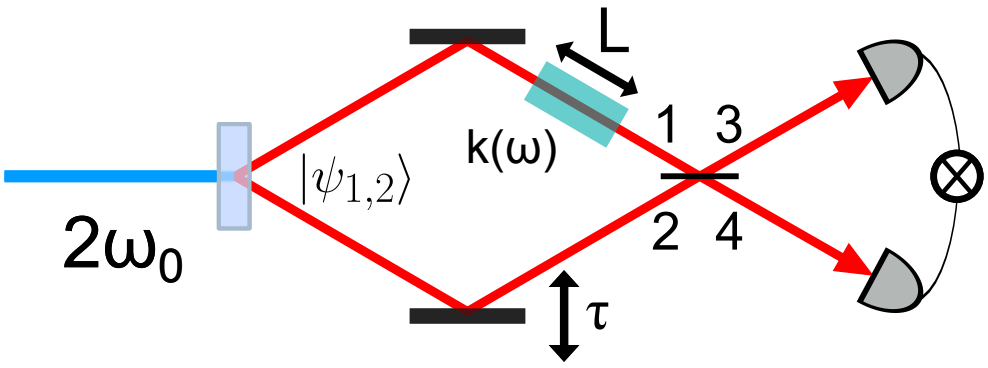

Figure 1.6: A Hong-Ou-Mandel interferometer. A narrowband laser of frequency $2\omega_0$ pumps a nonlinear crystal to produce broadband photon pairs (with state $|\psi_{1,2}\rangle$) via spontaneous parametric down-conversion. For each pair of photons produced, one travels through the sample arm of the interferometer and one travels through the reference arm. The dispersive element in the sample arm adds a phase $k(\omega)L$, and the reference arm adds a delay $\omega\tau$. When the path lengths of the interferometer are balanced the photons bunch at the beamsplitter and are emitted as a pair into either mode 3 or 4, and no coincidence counts are registered by the detectors.

energy conservation, $\omega_1 + \omega_2 = \omega_3$. The two-photon state $|\psi_{1,2}\rangle$ produced is

$$|\psi_{1,2}\rangle = \int d\omega_1 d\omega_2 f(\omega_1, \omega_2)|\omega_1\rangle|\omega_2\rangle \tag{1.37}$$

where $f(\omega_1, \omega_2)$ is the two-photon joint spectrum. For degenerate SPDC the two downconverted photons have frequencies centered at ω_0, and their joint spectrum can be modelled as [24]:

$$f(\omega_1, \omega_2) = \exp\left[-\frac{(\omega_1 - \omega_0)^2}{4\sigma^2}\right] \exp\left[-\frac{(\omega_2 - \omega_0)^2}{4\sigma^2}\right] \exp\left[-\frac{(\omega_1 + \omega_2 - 2\omega_0)^2}{4\sigma_c^2}\right] \tag{1.38}$$

The parameter σ_c can be thought of as the bandwidth of the pump photon, and this determines the strength of correlation between the two downconverted photons. When $\sigma_c/\sigma \ll 1$, the third exponential becomes extremely narrow, and the relation $\omega_1 + \omega_2 = 2\omega_0$ is enforced. In the opposite limit where $\sigma_c/\sigma \gg 1$, the joint spectrum becomes separable in the variables ω_1 and ω_2, and the photons become completely uncorrelated in frequency. We will show below that the QOCT signal is insensitive to quadratic dispersion in the high-correlation limit (i.e., when a narrowband pump photon is downconverted into a broadband photon pair). The bandwidths of the downconverted photons are related, but not equal, to σ. To read the bandwidth of photon 1, for example, photon 2 must be traced out of the state $|\psi_{1,2}\rangle$. In the high-correlation limit $\sigma_c/\sigma \ll 1$, the bandwidth of photon 1 is then $\sigma_1 = \sigma/\sqrt{2}$. In the low-correlation limit, tracing out photon 2 has no effect on photon 1, and a measurement would show that $\sigma_1 = \sigma$. A detailed discussion of the single-photon bandwidths can be found in section 3.2.1.

The photons can take two paths through the interferometer that lead to coincidence counts – both photons are either transmitted or reflected at the beamsplitter with amplitudes $A_{tt}(\omega_1, \omega_2, \tau)$ and $A_{rr}(\omega_1, \omega_2, \tau)$. Since the detectors count photon numbers, the coincidence signal is proportional to the square of the sum of these amplitudes [24]:

$$C(\tau) = \iint d\omega_1 d\omega_2 \left|A_{tt}(\omega_1, \omega_2, \tau) + A_{rr}(\omega_1, \omega_2, \tau)\right|^2 \tag{1.39}$$

The amplitudes depend on the phase acquired by each photon as it passes through the

interferometer. Applying the same phases as for the white-light interferometer above, but dropping the group-delay term (which only shifts the signal in the delay τ), the amplitudes are

$$A_{tt}(\omega_1, \omega_2, \tau) = f(\omega_1, \omega_2) e^{i\epsilon(\omega_1 - \omega_0)^2 + i(\omega_2 - \omega_0)\tau} \tag{1.40}$$

$$A_{rr}(\omega_1, \omega_2, \tau) = -f(\omega_2, \omega_1) e^{i\epsilon(\omega_2 - \omega_0)^2 + i(\omega_1 - \omega_0)\tau} \tag{1.41}$$

where $\epsilon = \beta L$ is the quadratic phase introduced by the material in the sample arm. Using the symmetry of the two-photon bandwidth function, $f(\omega_1, \omega_2, \tau) = f(\omega_2, \omega_1, \tau)$, and evaluating the integral gives a coincidence signal of:

$$C(\tau) \propto 1 - \sqrt{\frac{2\sigma^2 + \sigma_c^2}{2\sigma^2 + \sigma_c^2 + 4\epsilon^2\sigma^4\sigma_c^2}} e^{-\frac{\tau^2}{2} \frac{2\sigma^2(2\sigma^2 + \sigma_c^2)}{(2\sigma^2 + \sigma_c^2 + 4\epsilon^2\sigma^4\sigma_c^2)}} \tag{1.42}$$

This signal is a gaussian which has been subtracted from a constant background of coincidence counts. This produces a dip which has a width in time of:

$$\Delta\tau = \frac{1}{\sqrt{2}\sigma} \sqrt{1 + \frac{4\epsilon^2\sigma^4\sigma_c^2}{2\sigma^2 + \sigma_c^2}} \tag{1.43}$$

In the high-correlation limit, we have that $\sigma_c/\sigma \ll 1$ and $\sigma_c/(\epsilon\sigma^2) \ll 1$. Furthermore, in this limit the single-photon bandwidth is $\sigma_{sp} = \sigma/\sqrt{2}$ leading to a width of $\Delta\tau = 1/2\sigma_{sp}$. When the two photons are highly anticorrelated in frequency, the QOCT signal is insensitive to the presence of unbalanced quadratic dispersion. Furthermore, it is interesting to note that, for light sources with the same single-photon bandwidths, QOCT has a better resolution than WLI by a factor of two.

QOCT has two major disadvantages, the first being the QOCT signal is limited to very low powers. SPDC is a very inefficient process, as typically only 1 in every $10^6 - 10^8$ photons will be downconverted into a pair. Furthermore, photon pairs must be produced at a rate such that, with a high probability, at most only one photon pair will arrive at the detectors in the time period of the coincidence detection window. The fastest detectors currently available have coincidence windows on the order of 100 ps. The best

rates for the production and detection of entangled photon pairs is on the order of 10^6 pairs per second [2, 8]. The second disadvantage of QOCT is the presence of additional interference features in the signal called *artifacts* which can appear when a multilayer sample is imaged. The origin of these artifacts can be thought of as interference between the constant backgrounds of coincidence counts caused by reflections from different sample layers, and this interference can be either constructive or destructive (or somewhere in between). Artifacts occur between every pair of "real" signals corresponding to actual sample interfaces, and thus their number grows quadratically with the number of sample interfaces. In theory, artifacts can be filtered from the QOCT signal by using fast detectors with coincidence windows on the order of 10 fs, but this is infeasible with current technology. An in-depth discussion of the cause of artifacts in QOCT can be found in Section 2.7.1.

1.3.2 Chirped-pulse interferometry

Chirped pulse interferometry (CPI) is the time-reversed, classical analogue of QOCT. Frequency-anticorrelated pairs of laser pulses impinge on a beamsplitter, are sent through an interferometer, and are overlapped inside a nonlinear crystal where they undergo SFG [13, 24]. The signal produced by the setup in Figure 1.7 produces a dip when the interferometer arms are balanced. When the frequency anticorrelations are strong the dip is insensitive to unbalanced quadratic dispersion in the interferometer.

The frequency-anticorrelated pulses needed for CPI are created by oppositely chirping two halves of a laser pulse which has been split in half. If the pulses are chirped via the quadratic phase $\phi_{\pm}(\omega) = \pm A(\omega - \omega_0)^2$, their frequencies will vary linearly with time, following the function $\omega(t) \approx \omega_0 \pm t/(2A)$. The pulses are recombined on the input beamsplitter of the interferometer such that the center frequency ω_0 of both halves arrives at the beamsplitter at the same time. When the magnitude of chirp stretches the pulse to many times more than its transform-limited length (i.e., when $A \gg 1/\sigma^2$), the instantaneous frequencies of the two pulses will sum to a narrow band of frequencies centered around $2\omega_0$. When the interferometer arms are balanced, there are two processes which will produce this SFG light at $2\omega_0$; either antichirped light from the sample arm upconverts with chirped light from the reference arm, or vice versa. A source of background is SFG

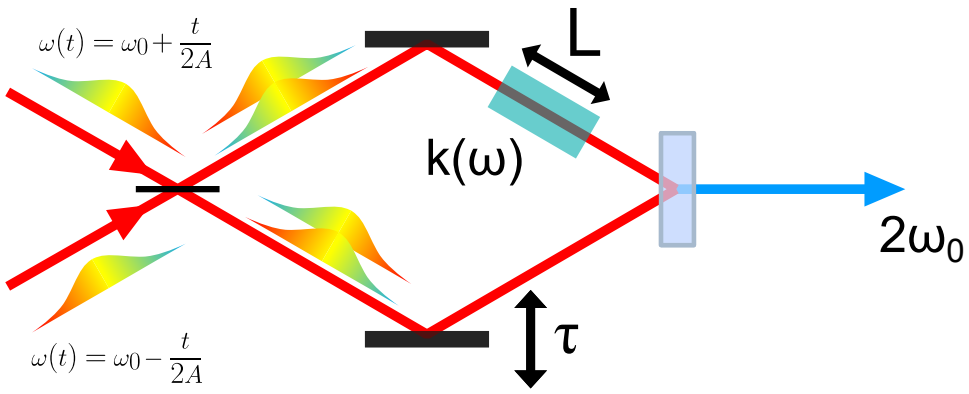

Figure 1.7: A chirped-pulse interferometer. A CPI set-up can be viewed as a time-reversed HOM-interferometer. Chirped and antichirped laser pulses are overlapped on a beamsplitter such that both beamsplitter outputs contain a superposition of a chirped and an antichirped laser pulse. The pulses are overlapped such that at any point along the superposition, the sum of the instantaneous frequencies is $2\omega_0$. After travelling through the interferometer the light is recombined on a nonlinear crystal where it undergoes SFG. The CPI signal is the intensity of SFG light near $2\omega_0$ as a function of the time delay τ.

light that is created by summing light that comes from the same interferometer arm. Due to conservation of momentum, this background will be in a different spatial mode than the CPI signal, and it can be filtered out spatially. This background has narrowband and broadband components created by upconverting oppositely- and identically-chirped components of the pulse, respectively. The broadband component of the background can be additionally filtered from the signal with a spectrometer. The CPI signal is the intensity of SFG light measured as a function of reference-arm delay, and the electric field amplitude of this light is given by the convolution of the fields in the sample and reference arm:

$$E_{signal}(\omega) \propto \int d\omega' E_1(\omega') E_2(\omega - \omega') \tag{1.44}$$

The chirped and antichirped fields are given by $E_{\pm}(\omega) = \mathcal{E} e^{-\frac{(\omega-\omega_0)^2}{4\sigma^2}} e^{i\phi_{\pm}(\omega)}$, and the fields collect the usual phases from the sample and reference arms. Hence, E_1 and E_2 are given by:

$$E_1(\omega) = \left[E_+(\omega) + E_-(\omega)\right] e^{i\epsilon(\omega-\omega_0)^2} \tag{1.45}$$

$$E_2(\omega) = \left[E_+(\omega) - E_-(\omega)\right] e^{i\omega\tau} \tag{1.46}$$

$$\tag{1.47}$$

where once again the group delay term has been dropped and $\epsilon = L\beta$. The SFG field is then:

$$\begin{aligned} E_{signal}(\omega,\tau) \propto \int d\omega' \Big\{ & E_+(\omega')E_+(\omega-\omega') + E_-(\omega')E_-(\omega-\omega') \\ & + E_-(\omega')E_+(\omega-\omega') - E_+(\omega')E_-(\omega-\omega') \Big\} e^{i\epsilon(\omega'-\omega_0)^2} e^{i(\omega-\omega')\tau} \end{aligned} \tag{1.48}$$

$$\approx \int d\omega' \left[E_-(\omega')E_+(\omega-\omega') - E_+(\omega')E_-(\omega-\omega')\right] e^{i\epsilon(\omega'-\omega_0)^2} e^{i(\omega-\omega')\tau} \tag{1.49}$$

The first two terms in (1.48) describe a broadband SFG background, and the remaining two terms describe higher-intensity, narrowband SFG at $2\omega_0$. The narrowband light forms the majority of the signal at frequencies near $2\omega_0$, and if the SFG is spectrally filtered

near $2\omega_0$, the SFG field can be approximated by dropping the broadband terms. The CPI signal is thus the measured intensity of the narrowband light, which is expressed as:

$$I(\tau) = \int d\omega \, |E_{signal}(\omega, \tau)|^2 \tag{1.50}$$

Evaluating the integrals and taking the large-chirp limit where $A \gg 1/\sigma^2$ is satisfied gives a CPI signal of:

$$I(\tau) \propto 1 - \exp\left[-\frac{\tau^2}{2}\frac{8\sigma^6(1+2(2A^2+\epsilon^2)}{16A^2\sigma^4+(1+8\epsilon^2\sigma^4)^2}\right] \tag{1.51}$$

which is a constant background with a dip at $\tau = 0$, similar to the QOCT signal. The width of this dip is:

$$\Delta\tau = \frac{1}{\sqrt{2}\sigma}\sqrt{1+4\epsilon^2\sigma^4\left(\frac{2+16\epsilon^2\sigma^4}{1+16A^2\sigma^4+8\epsilon^2\sigma^4}\right)} \tag{1.52}$$

The resolution-degrading effects of dispersion are minimized by chirping the two beams. When the chirp is much larger than the unbalanced dispersion (i.e., when $A \gg \epsilon$), the CPI dip-width is $\Delta\tau = 1/\sqrt{2}\sigma$, which is insensitive to quadratic dispersion.

CPI has an advantage over QOCT in that it can be much more efficient. In practice, SFG can have very high efficiency with short laser pulses, but SPDC can not. Furthermore, the maximum power of the CPI signal isn't limited by coincidence detection. Early demonstrations of CPI produced a signal with an intensity that was $\sim 10^7$ times greater than that acheivable with QOCT [13, 15]. Artifact signal features are present in CPI, however they are spectrally separated from the main CPI signal at $2\omega_0$. Hence, as explained in Section 2.7.1, they can be easily filtered from the signal with a spectrometer.

Chapter 2

Dispersion-cancelled biological imaging with quantum-inspired interferometry

2.1 Notes and acknowledgements

In this chapter we use a chirped-pulse interferometry system to image a biological sample, namely, the cells of an onion. This is a proof-of-principle experiment with the goal of demonstrating the first dispersion-cancelled image of the interior of a biological sample. We were able to image the interior structure of an onion to a depth of about 0.5 mm with a resolution of a few microns. The image resolution wasn't degraded by the quadractic dispersion introduced from a 3-mm-thick BK7 glass window placed in front of the sample. Furthermore, we were able to filter all artifacts out of our signal, allowing us to produce clear, uncluttered images.

Notice

The content of this chapter has been published in:

M. D. Mazurek, K. M. Schreiter, R. Prevedel, R. Kaltenbaek, and K. J. Resch. Dispersion-cancelled biological imaging with quantum-inspired interferometry. *Scientific Reports* **3**, 1582

Author Contributions

Kevin Resch and **Rainer Kaltenbaek** conceived of the experiment.

Kurt Schreiter, **Rainer Kaltenbaek**, and **Robert Prevedel** set up the pulse shaper and cross correlator and performed preliminary experiments.

Kurt Schreiter wrote the control software and calibrated the SLM.

Michael Mazurek modified the setup and performed the experiments and simulations presented here, and along with **Robert Prevedel** analyzed the data.

Michael Mazurek and **Kevin Resch** wrote the first draft of the manuscript.

All authors contributed to the final version.

2.2 Overview

Quantum information science promises transformative impact over a range of key technologies in computing, communication, and sensing. A prominent example uses entangled photons to overcome the resolution-degrading effects of dispersion in the medical-imaging technology, optical coherence tomography. The quantum solution introduces new challenges: inherently low signal and artifacts, additional unwanted signal features. It has recently been shown that entanglement is not a requirement for automatic dispersion cancellation. Such classical techniques could solve the low-signal problem, however they all still suffer from artifacts. Here, we introduce a method of chirped-pulse interferometry based on shaped laser pulses, and use it to produce artifact-free, high-resolution, dispersion-cancelled images of the internal structure of a biological sample. Our work fulfills one of the promises of quantum technologies: automatic-dispersion-cancellation interferometry in biomedical imaging. It also shows how subtle differences between a quantum technique and its classical analogue may have unforeseen, yet beneficial, consequences.

2.3 Introduction

Quantum information science promises powerful and unconventional capabilities across a broad range of technologies. An important example relates to the imaging technology, optical coherence tomography (OCT). OCT can noninvasively reconstruct the 3-dimensional structure of tissue with micron resolution [23]; it is emerging as an important clinical tool with diverse medical applications. OCT can diagnose retinal diseases such as glaucoma, analyze artherosclerotic tissues within arteries, and detect early-stage cancerous lesions in breast tissue [9, 33]. In addition, OCT has found application in precision laser machining [31]. Since OCT relies on low-coherence interferometry, its axial resolution is limited by the coherence length of the light, inversely proportional to the bandwidth. The coherence length determines ultimate resolution, however material dispersion can limit the practical one.

Fundamental studies in quantum optics showed that interference with energy-time entangled photon pairs [12] exhibits inherent robustness against unbalanced dispersion [27, 28]. Even-order effects of dispersion, including the dominant group-velocity dispersion, are automatically cancelled, effectively solving the dispersion problem. This dispersion cancellation is *automatic* since one does not need to precisely measure and compensate the dispersion. When energy-time entanglement is strong, but not perfect, the effect is more accurately described as automatic even-order dispersion *reduction* since the dispersion is dramatically reduced, not cancelled [24]. OCT based on entangled-photon interferometry was proposed to harness automatic dispersion cancellation [1]. This *quantum*-optical coherence tomography (QOCT) has two significant barriers to practical implementation. Firstly, the reliance on producing and resolving individual photon pairs places stringent limits on the QOCT signal using state-of-the-art systems [2, 8]. Secondly, in samples with multiple interfaces, QOCT produces a signal for each interface *and* an additional, artifact feature for each unique *pair* of interfaces [1, 20, 29]; the number of artifacts grows quadratically with the number of interfaces, cluttering the image of complex samples. QOCT was first used to perform an axial scan of a coverslip [20] and later applied to measure the surface topography of a gold-coated onion sample [19]. The gold coating was essential to increase reflectivity but rendered the technique impractical for *in vivo* applications; furthermore,

it prevented imaging the sample's internal structure, which is one of the main benefits of OCT and necessary for most medical applications.

Recently, several different approaches have shown that dispersion cancellation does not require entanglement, but can also be observed in classical systems [3, 7, 11, 13, 25]. While all of these methods could, in principle, solve the low-signal problem of QOCT, each suffers from unwanted artifacts. Here we focus on one of these techniques, chirped-pulse interferometry (CPI). A method for identifying artifacts in CPI has been demonstrated, but it requires multiple axial scans of a sample and is thus inherently slow [15].

In the present work, we describe and demonstrate a new method for CPI using a single beam of shaped laser pulses. Our method produces background-free, dispersion-cancelled signals, completely free of artifacts without multiple scans. We apply this technique to image a biological sample, demonstrating dispersion cancellation and observing the sample's internal structure. CPI overcomes both limitations of QOCT while retaining its advantages, demonstrating its potential for future practical application.

2.4 Results

2.4.1 Theoretical description.

CPI uses classical light with strong frequency anti-correlations. To create these anti-correlations, we constructed a 4-F pulse shaper with a spatial light modulator (SLM) [32, 16]. In CPI, this method has distinct advantages over pulse-stretching techniques with bulk optics [22, 17], including: straightforward optimization of the chirp parameter [24], better stability and efficiency, and more complex pulse shapes. We apply a frequency-dependent phase shift to the laser pulses, $\phi(\omega) = -A(\omega - \omega_0)|\omega - \omega_0|$, where A is a positive constant. The absolute value distinguishes this from the quadratic phase leading to linear chirp: $\phi(\omega)$ applies a linear chirp to red-shifted frequencies ($\omega < \omega_0$) and an equal, opposite chirp (antichirp) to blue-shifted frequencies ($\omega > \omega_0$). The resulting pulse has frequency ω_0 at its lagging edge, and instantaneous frequencies in the preceding part of the pulse obey the function $\omega(t) \approx \omega_0 \pm \frac{t}{2A}$ $(-\infty < t \leq 0)$. These are the frequency anti-correlations needed

for CPI. We refer to this as a Blue-Antichirped-Red-Chirped (BARC) pulse.

CPI can be understood by considering the schematic in Figure 1a. Light in the upper arm of the interferometer travels through a dispersive material of length L as well as a distance $L_1 - L$ through free space; light in the lower arm travels a distance L_2 through free space. The dispersive material in the upper arm has a wavevector of light that can be expanded about frequency ω_0 as $k(\omega) = k(\omega_0) + \alpha(\omega - \omega_0) + \beta(\omega - \omega_0)^2 + \ldots$, where α and β describe the group delay and group velocity dispersion, respectively. At any time, two laser beams with frequencies $\omega_0 + \Delta$ and $\omega_0 - \Delta$ enter the interferometer with corresponding amplitudes $E(\Delta)$ and $E(-\Delta)$. After travelling through the interferometer they overlap at the nonlinear crystal for sum-frequency generation (SFG). Two paths produce SFG with frequency $2\omega_0$; either blue-shifted light travels the upper arm and red-shifted light travels the lower arm, or vice versa. The amplitudes for these two paths interfere to give a signal $S(\Delta, \tau) = |E(\Delta)E(-\Delta)|^2 \left(1 + \cos\left[\phi_+(\Delta, \tau) - \phi_-(\Delta, \tau)\right]\right)$, where $\tau = (L_2 - L_1 + L)/c$ is the time delay between the two paths [13]. To second order in the wave-vector and ignoring a global phase, the respective phases of the two paths are, $\phi_\pm(\Delta, \tau) = L(\pm\alpha\Delta + \beta\Delta^2) \mp \Delta\tau$. The final signal results from integrating Δ over the pulse bandwidth, forming a peak at $\tau = \alpha L$ [14]. Since unbalanced dispersion contributes the same phase $\beta\Delta^2$ to each path, the effect cancels out of the final signal; this is automatic dispersion-cancellation. With imperfect anti-correlations, dispersion cancellation persists if the unbalanced dispersion is much less than the chirp parameter, A [24].

Ideally, each interference signal would correspond to an interface in the sample. However, in both QOCT [20] and CPI [15] an additional artifact signal appears halfway between the signals arising from each pair of interfaces. In complex samples, artifacts can outnumber the features from real interfaces, seriously impeding reconstruction and interpretation. The origin of the artifacts in these two techniques are subtly, but importantly different (see Figure 2.5). Artifacts in CPI are a result of interference in the SFG light at frequencies blue-shifted or red-shifted from the operating frequency, $2\omega_0$, by an amount $\Delta\omega = \Delta\tau/(4A)$, where $\Delta\tau$ is the time-delay difference between the two sample interfaces. Spectral filtering of the SFG can remove all artifacts arising from pairs of interfaces separated by more than some minimum delay. The analogous method of artifact removal in QOCT requires coincidence detection with tens of femtoseconds time-resolution, which is

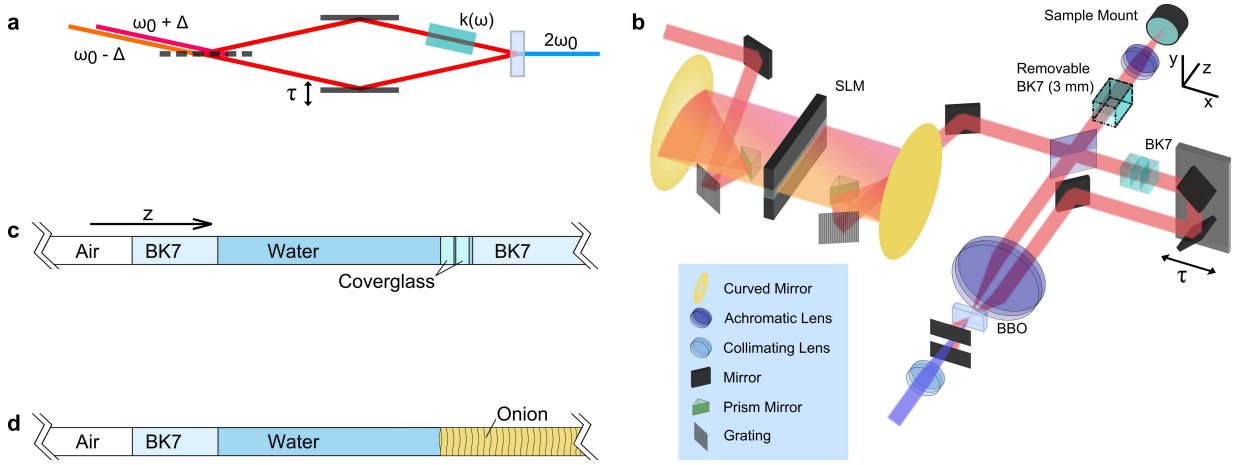

Figure 2.1: An optical-coherence-tomography system based on chirped-pulse interferometry. **a** A simplified schematic of CPI. A common-mode pair of classical beams with anticorrelated frequencies impinges on a beamsplitter and the two resulting paths overlap in a β-barium borate (BBO) crystal for sum-frequency generation (SFG) after one path experiences a variable delay, τ, and the other passes through a dispersive material which has frequency-dependent wave-vector $k(\omega)$. The frequency offset, Δ, is swept over the bandwidth of the input pulses. The CPI signal then is the intensity of the SFG light near $2\omega_0$ as a function of τ. This signal is inherently robust against unbalanced dispersion. **b** The experimental implementation. Broadband pulses from a titanium:sapphire laser pass through a 4-F pulse-shaper, [32, 16] the light is then split into a beam that reflects from the sample in the focus of a lens, and a beam that travels a variable-length delay. The delay and the x- and y-positions of the sample are motorized. A stack of BK7 glass in the reference arm introduces dispersion equal to that of the static optical elements in the sample arm, including the BK7 window and water layer in the sample holder, but excluding the samples themselves. The pulse shaper compensates for this static, balanced dispersion throughout the experiment such that the laser pulse is transform limited at the nonlinear crystal. The pulse shaper can add an additional phase shift, $\phi(\omega)$, to produce the BARC pulse shape at the crystal. Inserting an extra 3 mm-thick BK7 window in the sample arm introduces a controlled amount of unbalanced dispersion. Light from the two interferometer arms is focused onto a nonlinear crystal and undergoes non-collinear SFG. The SFG light passes through a spatial filter and a monochromator, and the signal is measured as a function of time delay using a photomultiplier. Illustration of the cross-sections of the two samples, **c** microscope coverglass slides and **d** a piece of onion. Each sample was held in a lens tube, and placed behind a layer of distilled water and a 1 mm thick BK7 window; the 2.7 mm water layer prevented drying of the onion sample.

extremely difficult in practice.

2.4.2 Experimental setup and characterization.

Our experimental set-up is shown in Figure 2.1b. We used this system to image a stack of two microscope coverglass slips (Figure 2.1c) and an onion (Figure 2.1d). First, we focus on the coverglass sample to benchmark our system performance. We measure the SFG power as a function of time delay, τ, with two types of pulses, a transform-limited (TL) pulse and the BARC pulse. Using the TL pulse is equivalent to OCT with background-free autocorrelation [21], which does not suffer from artifacts but is not dispersion cancelling. In order to remove artifacts from signals acquired with BARC pulses the SFG signal is sent through a 0.35 nm bandwidth filter. See Methods for more details.

The data measured using TL and BARC pulses are shown in Figures 2.2a and b, respectively. Black (red) lines show data without (with) unbalanced dispersion from 3 mm BK7 in the sample arm, where the light passes twice through the glass. The left-most four peaks correspond to the front and back surfaces of the first and second coverglass pieces. The average delay between the first (second) two peaks is $248 \pm 4\,\mu$m ($236 \pm 4\,\mu$m). Dividing by the group index $n_g = 1.517$ of the coverglass gives thicknesses of $163\,\mu$m and $156\,\mu$m for the two slides, in good agreement with $164 \pm 3\,\mu$m and $157 \pm 3\,\mu$m measured with a caliper. We subtracted a constant 1.6 mm from the delay-arm motor position in the unbalanced-dispersion data to compensate for the group delay from the additional glass so corresponding peaks could be overlayed for comparison.

Figures 2.2a and b show that no additional artifact features arise going from a TL to a BARC pulse. In section 2.7.1, we show the maximum layer separation giving rise to artifacts is $3\,\mu$m, narrower than the peak widths, $4.2\,\mu$m. As expected, any resolvable artifacts are filtered out of our signal.

The average signal peak width for the TL pulses is $3.6 \pm 0.2\,\mu$m (FWHM) which broadened by 106% to $7.4 \pm 0.6\,\mu$m by the dispersion. Uncertainties represent the standard deviations of the five peak widths. In contrast, the BARC-pulse produced average signal widths of $4.2 \pm 0.1\,\mu$m that broadened by only 7% to $4.5 \pm 0.2\,\mu$m, demonstrating dispersion cancellation. The measured peak widths for the TL and BARC pulses are in good

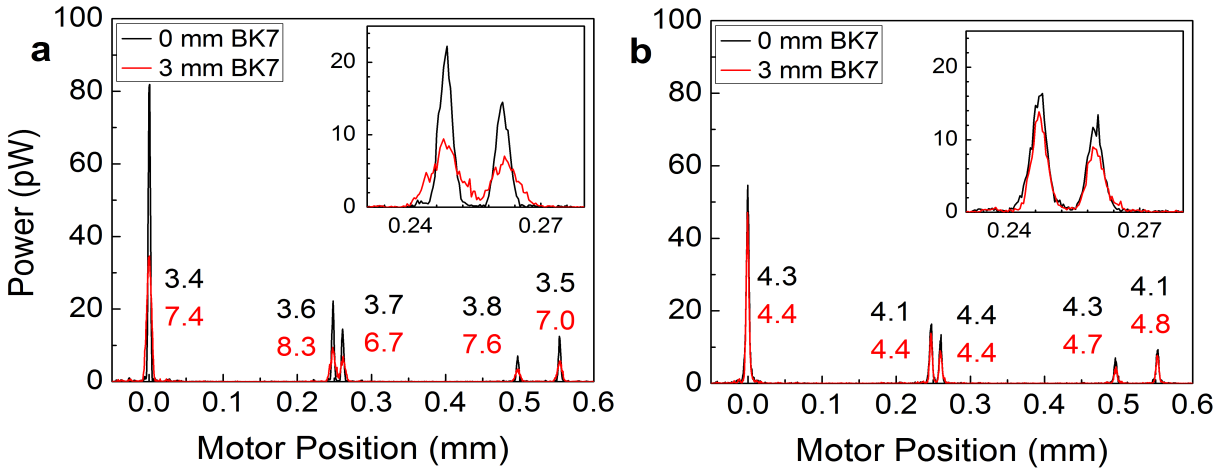

Figure 2.2: Axial scans of the coverglass sample using **a** transform-limited pulses and **b** BARC pulses. Each set of data shows five distinct peaks; the left-most four arise from the front and back surfaces of each of the two coverglass slides while the final right-most peak is from the BK7 base of the sample holder. Each peak is associated with a real interface and the BARC-pulse signal shows no additional features as compared with **a**. Thus any artifacts have been effectively removed by our filtering technique. The black (red) data were taken without (with) the removable 3 mm BK7 in the sample arm. The numerical labels denote each peak width in microns (FWHM). The peaks in **a** from the transform-limited pulses were broadened by 106% from the unbalanced dispersion, while that in **b** from the BARC pulses were broadened by just 7%. Dispersive broadening can be observed directly by zooming in on the pair of peaks near motor position 0.25 mm shown in the insets. These data demonstrate automatic dispersion cancellation in our chirped-pulse interferometer.

agreement with the theoretical calculations of 3.4 μm and 4.1 μm, respectively, using the 60 nm acceptance bandwidth of our system. The peak width of the BARC-pulse signal is broadened compared to the TL pulses as a result of the narrow filtering of the SFG; if a broader bandwidth was measured instead, the widths become equal, but artifacts can reappear. The dispersion cancellation observed cannot be explained by the slightly broader BARC-pulse signal in the balanced dispersion case. If one used a TL pulse yielding a 4.2 μm peak width in the absence of dispersion, equal to the width to our BARC-pulse signal, we calculate that two passes through 3 mm BK7 glass would broaden the signal to 5.8 μm, a 38% increase. Our BARC-pulse signal is broadened by 7%, thus the dispersion cancellation is significant even when compared with this conservative benchmark.

2.4.3 Dispersion-cancelled biological imaging.

We prepared a sample of onion as depicted in Figure 2.1d and took a set of axial (z) scans, moving the sample in the y-direction between scans. The data are displayed in Figure 2.3, where the four panels a, b, d, and e show cases with and without dispersion (3 mm BK7) for both TL and BARC pulses. The vertical axes are the delay-arm motor positions and the horizontal axes show the transverse y-positions. The images show the cellular structure of the onion deep into the sample and are artifact-free. Beside each image, we show a single axial scan taken at the y-position marked by the red line in each plot. The TL-pulse signal peaks are dramatically broadened when unbalanced dispersion is added, but the BARC-pulse peak widths are unchanged, directly demonstrating automatic dispersion cancellation in our image. In order to compare the effect of dispersion over the entire images produced by the TL pulses and BARC pulses, we recorded the widths of signal peaks throughout the images and display corresponding histograms in Figures 2.3c and f. The TL-pulse peaks broadened by 61% from an average of $3.6 \pm 0.5\,\mu$m to $5.7 \pm 1.2\,\mu$m, where uncertainties are the standard deviations of each distribution. The BARC-pulse peak widths increased by only 4% from $4.2 \pm 0.8\,\mu$m to $4.3 \pm 0.6\,\mu$m, less than the standard deviation. Hence, dispersion is cancelled througout the BARC-pulse images.

To further show the capability of our method, we took a set of axial (z) scans over a grid of x- and y-positions of a different onion sample prepared in the same manner as before,

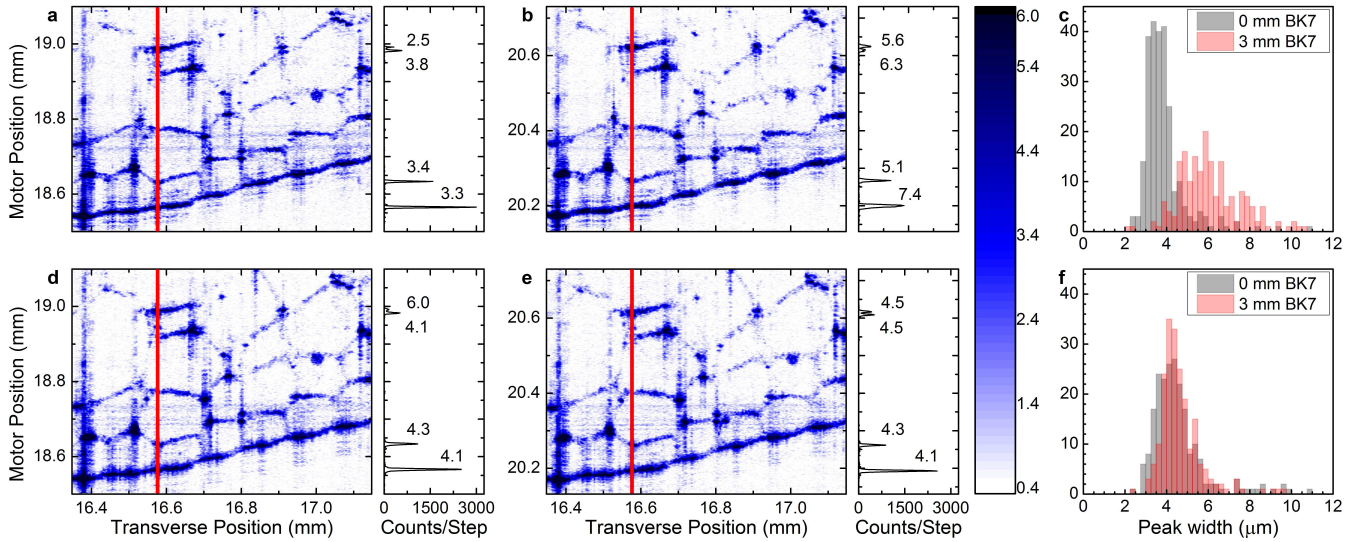

Figure 2.3: Two-dimensional images of an onion sample. Panel **a** was taken with the TL pulse with no unbalanced dispersion, **b** TL pulse with 3 mm of BK7 in the sample arm for unbalanced dispersion **d** BARC pulse, no dispersion, and **e** BARC pulse with unbalanced dispersion. The colour-bar represents the natural logarithm of the number of counts per delay-arm motor step recorded by the photomultiplier. The internal cellular structure of the onion is visible deep into the sample in all four images and comparing the images we see that no artifacts are introduced by using BARC pulses. A single axial scan at the transverse position indicated by the red vertical line in each image are plotted on a linear scale beside each corresponding image; the labels represent the widths of each peak FWHM in micrometres. The addition of dispersion significantly broadens the TL-pulse peaks while in contrast the BARC-pulse peaks are dispersion cancelled. Peak widths over each entire image are plotted as histograms shown in panels **c** and **f**, for the TL and BARC pulses respectively; the black bars are used for no unbalanced dispersion and the red for unbalanced dispersion. The peak widths for the TL pulses broadened by 61% with the addition of dispersion, while those from the BARC pulses broadened only by 4%. Dispersion cancellation is thus achieved over the entire image.

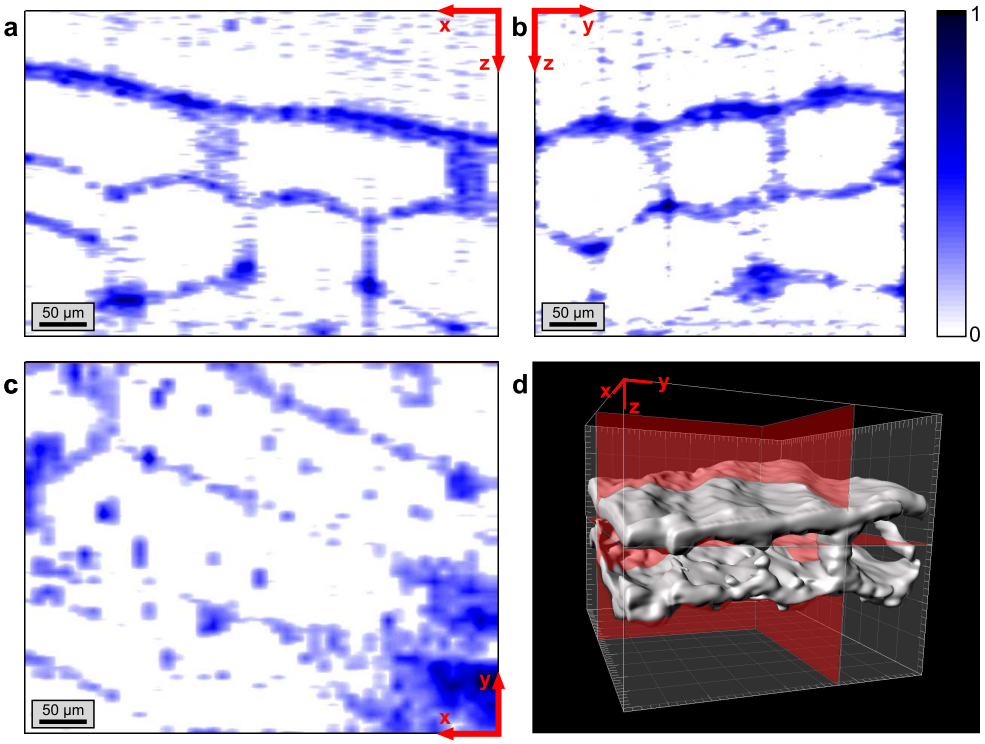

Figure 2.4: A three-dimensional image of an onion sample. Using BARC pulses with no unbalanced dispersion, we took a set of axial (z) scans at a grid of x- and y-positions on an onion sample. Panels **a**, **b**, and **c** show 2D cross-sectional images of our 3D data in the xz, yz, and xy planes depicting the cellular structure. In panel **d**, we show a 3D rendering of the surface layer of cells extracted from our data. The grid spacing is 50 μm, and the transparent red planes correspond to the slices shown in panels **a**, **b**, and **c**.

using the BARC pulses with no unbalanced dispersion. From this data, we extracted 2D cross-sections of the sample shown in Figures 2.4a–c and the 3D cell wall structure of the top layer of cells is shown in Figure 2.4d. Thus CPI, with its inherent dispersion cancellation, is suitable for practical 3D imaging of biological samples.

2.5 Discussion

We have demonstrated dispersion-cancelled, artifact-free, optical-coherence-tomography imaging of a biological sample. For future work, incorporating a nonlinear material with larger nonlinearity and acceptance bandwidth [21, 18] will improve the system, increasing acquisition rates and image resolution. Dispersion-cancelled OCT with chirped-pulse interferometry draws upon insights from quantum information science. Exploiting subtle differences in the analogous roles played by different physical parameters between the techniques allowed problems inherent to the quantum scheme to be solved in the classical technology; what is very hard, or even technologically impossible, in the quantum device becomes straightforward in CPI. Our results remove the technological barriers to dispersion-cancelled biological imaging and underscore the importance of understanding classical analogues to quantum mechanical effects.

2.6 Methods

Pulses from a titanium:sapphire laser (808 nm, 90 nm FWHM) pass through a 4-F pulse shaper incorporating a spatial light modulator (CRi SLM-640-D-VN) [32, 16], also see [26] for details. The SLM served two purposes, compressing the pulses by compensating for balanced dispersion in the setup, and applying the BARC-phase $\phi(\omega) = -A(\omega-\omega_0)|\omega-\omega_0|$, where $A = 2500\,\mathrm{fs}^2$ and $\lambda_0 = 2\pi c/\omega_0 = 809.60\,\mathrm{nm}$. The shaped pulses were split on a beamsplitter with 16 mW sent to the sample and 24 mW into a variable-delay line (a retroreflector on a motorized stage). A 3 mm thick BK7 glass window could be inserted into the sample arm to introduce unbalanced dispersion of $\beta = 132\,\mathrm{fs}^2$. A small onion sample was placed inside a 1″ lens tube, submerged in water, covered with a 1 mm-thick

BK7 window (Figure 2.1d), and mounted on a motorized x-y stage. A washer separated the onion and BK7 window by 2.7 mm. A 19 mm achromatic lens on a motorized stage focused the beam inside the sample to a spot size of approximately 6 μm. The delay-arm and sample-arm beams were focused using a 75 mm achromatic lens onto a 0.5 mm BBO crystal, cut for type-I SFG. The beam separation at the lens was 14 mm. The SFG signal was collimated and sent through a monochromator (Princeton Instruments Acton Advanced SP2750A) and detected with a single-photon-counting photomultiplier (Hamamatsu H10682-210). The monochromator was centred at 404.80 nm when the TL-pulse was used, and 404.64 nm when the BARC-pulse was used, to account for a small shift in the signal frequency induced by the added dispersion (see Figure 2.6). The acceptance bandwidth of the monochromator was 0.35 nm in both cases. This filtering of the SFG light was performed in order to remove artifacts from signals acquired with BARC pulses.

Axial depth scans were taken by moving the retro-reflector and recording the photomultiplier signal every 0.4 μm. For the cover-glass samples, the delay-stage speed was 0.5 mm/s and the delay stage scanned a range of 700 μm. For the 2D onion data, axial scans were taken over an 800 μm range in the y-direction with one scan every 4 μm. The delay-stage speed was 0.1 mm/s and it was scanned over a total range of 600 μm. The acquisition time per image was 1 hour.

For the histograms in Figure 2.3, all peaks from each axial scan were fitted provided their amplitudes were between 250 and 6000 counts per delay-stage step, so that their widths were not obscured by noise or detector saturation. Each histogram was fit with a Gaussian peak to estimate the mean and variation of the peak widths in each image.

The 3D onion data was taken over a range of 300 μm, 500 μm, and 350 μm in the x, y, and z directions, respectively. One axial scan was taken every 10 μm in the x and y directions. Every five data points in the z direction were binned to provide a point every 2 μm. Smoothing and threshold algorithms were applied to the raw data to create the 2D images. The 3D structure was visualized with the Imaris (Bitplane, Inc.) software after an FFT bandpass filter was applied. The delay-stage speed was 0.3 mm/s and data acquisition took 2.5 hours.

2.7 Supplementary Information

2.7.1 Artifacts in Quantum and Chirped-pulse optical coherence tomography

Conventional time-domain optical coherence tomography (OCT) is based on white-light interferometry [9]. The signal produced from such an interferometer exhibits an interference feature whenever the group delay for the reference arm matches that in the sample arm for one of the interfaces in the sample. Thus for a sample with N interfaces, one expects N features in the resulting interferogram.

Quantum-optical coherence tomography (QOCT) [1] and a previous implementation of chirped-pulse interferometry (CPI) [15] behave differently in that they produce not only these features, but also additional features which we refer to as *artifacts*. Due to the very strong analogy between QOCT and CPI, the origins of these artifacts are similar, but there are important differences, both fundamental and practical. As we will show in the following, this subtle difference allows for a relatively simple way for suppressing the artifacts in CPI while a corresponding approach in QOCT proves to be impossible with state of the art technology.

Figure 2.5a depicts a QOCT system based on a Hong-Ou-Mandel interferometer [12]. Pairs of energy-time entangled photons are generated by spontaneous parametric down-conversion (SPDC) of a narrow band pump laser. Perfectly energy-time entangled photons have the property that photon pairs are produced simultaneously, but without an absolute time reference. In other words, one cannot predict when one will detect one of the photons from each pair. However, once one photon is detected, the other will be detected at the same time. As a result of this property, interference with energy-time entangled photons depends only on the difference in detection times, not on the absolute detection time.

In its most simple form, Hong-Ou-Mandel interference occurs when the delays between the two arms of the interferometer are balanced and the photons arrive at the detectors simultaneously; when there are multiple interfaces in one of the arms, one expects interference whenever the delay in the reference arm matches that from one of the interfaces.

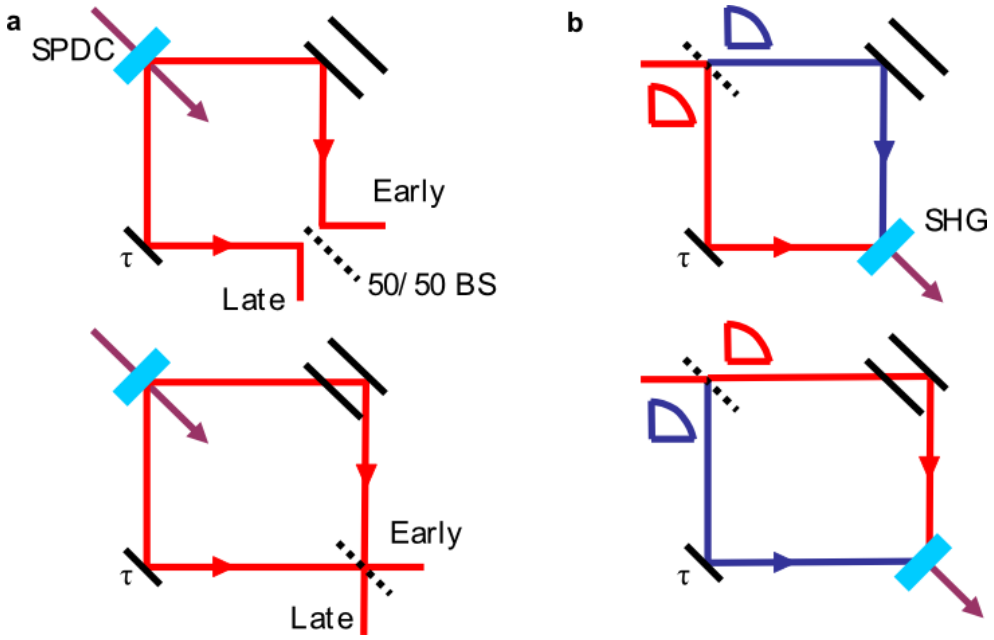

Figure 2.5: Interfering paths that lead to artifacts in QOCT and CPI. **a** depicts a QOCT setup. When the path length of the reference arm is the average of the paths in the sample arm for the two interfaces, two indistinguishable early/late coincidences will occur. The indistinguishable paths in CPI are shown in **b**. The SFG signal from these two paths will be the same frequency when the delay matches the average of the delays for the two interfaces in the sample arm, leading to an artifact between the "real" features corresponding to the two sample interfaces.

This interference gives rise to signal features at the same delays as standard white-light interferometry [1], and they correspond to the actual interfaces in the sample.

Artifacts, on the other hand, arise from the interference when the photons do not arrive at the detectors simultaneously, but rather with a well defined time difference. The upper diagram in Fig. 2.5a depicts one path leading to an early photon at output 1 and a late photon at output 2. If the delay for light reflecting from the first interface is τ_1, then the expected time difference in the detections is $\tau_1 - \tau$. The lower diagram shows a different path leading to an early detection at output 1 and a late one at output 2. If the delay from the second interface is τ_2, then the time difference is $\tau - \tau_2$. These time differences are equal when

$$\tau_1 - \tau = \tau - \tau_2 \tag{2.1}$$

$$\tau = (\tau_1 + \tau_2)/2. \tag{2.2}$$

When the reference arm delay is set to the average of the delays for the two interfaces, the time differences between the detections for these two paths are equal. In this case, the paths are indistinguishable, leading to two-photon interference and the corresponding formation of artifacts [29, 1, 20]. We can express this time difference between the early and late photon detections as $\Delta\tau = (\tau_1 - \tau_2)/2$.

Unlike the signals in the HOM interferometer corresponding to actual interfaces, the amplitude of these artifacts is phase sensitive. Depending on the phase, the amplitude of each artifact can be positive, negative, or even vanish completely. If an artifact occurs at the same position as the signal from a real interface, and if the amplitude is negative, an artifact can even cancel a real signal. For a simple two-interface structure, like the one shown in Fig. 2.5, there is only a single artifact, but the number of artifacts grows as the number of distinct pairs of interfaces $N(N-1)/2$, quadratically for large N. In complex samples, the high number of artifacts poses a significant challenge for QOCT because artifacts may be mistaken for or cancel real signals.

If one could limit observations to only those photon pairs that are exactly coincident, then one could, in principle, avoid artifacts altogether. However, since detector jitter and coincidence windows for state-of-the-art detectors are typically on the order of a few hun-

dred picoseconds, only those artifacts from interface pairs with a distance on the centimeter length scale could be avoided in this way. One would need to reduce that timescale to tens of femtoseconds (three orders of magnitude better than state-of-the-art) to avoid artifacts for interface-pairs separated by distances on the micrometer length scale relevant for OCT imaging.

Now consider Fig. 2.5b which depicts the same, double-interface sample in CPI based on BARC-pulses. For large chirp, the BARC-pulse can be viewed as a superposition where the red-shifted part of the spectrum ($\omega < \omega_0$) is linearly chirped such that $\omega_R(t) = \omega_0 + \frac{1}{2A}t$ for $t < 0$, where A is a positive number, and the blue-shifted half of the spectrum ($\omega > \omega_0$) is anti-chirped such that $\omega_B(t) = \omega_0 - \frac{1}{2A}t$ for $t < 0$. We expect the lagging edge of the pulse to have instantaneous frequency ω_0 and to arrive at $t = 0$ with the rest of the pulse arriving earlier, i.e., at negative times t.

For CPI, peaks will appear in the signal whenever the two interferometer arms are balanced. For a multi-interface sample, multiple peaks will appear as the reference arm is scanned; these peaks are in the same locations as the dips in the HOM signal [15].

To understand the origin of the artifacts in CPI, we consider the two paths shown in Fig. 2.5b. In the upper diagram, the blue part of the spectrum reflects from the front interface and experiences a delay τ_1 on its way to the crystal, the red part of the spectrum traverses the reference path and experiences a delay τ. The expected frequency of the SFG signal for this path is $\omega_B(t+\tau_1)+\omega_R(t+\tau) = 2\omega_0 + \frac{1}{2A}(\tau - \tau_1)$. Similarly, the frequency of the SFG signal for the path in the lower diagram is $\omega_B(t+\tau)+\omega_R(t+\tau_2) = 2\omega_0+\frac{1}{2A}(\tau_2-\tau)$. These frequencies are equal when, $\tau = (\tau_1 + \tau_2)/2$, i.e., when the reference delay is equal to the average of the delays for the front and back surfaces; this condition is identical to the one for artifacts in QOCT.

An essential difference is that the physical signature for the artifact in CPI is a frequency shift with respect to $2\omega_0$ in the SFG signal rather than a difference in relative arrival time of the photons as in QOCT. If we set $\tau = \frac{(\tau_1+\tau_2)}{2}$, we can calculate the expected frequency shift for artifacts with respect to $2\omega_0$, the frequency of the signals corresponding to actual

interfaces:

$$\Delta\omega = \frac{1}{2A}\frac{(\tau_1 - \tau_2)}{2}. \tag{2.3}$$

Note that swapping the roles of the red and blue parts of the spectrum leads to a second artifact at the same delay position but with an opposite frequency shift of $-\Delta\omega$.

The artifact signatures in CPI have the same dependence on path delays as in QOCT, except that they are converted into a frequency shift depending on the chirp parameter, A. Artifacts will be visible in the CPI interferogram if the corresponding frequency shift lies within the monochromator acceptance bandwidth $\Delta\Omega$ around $2\omega_0$. Substituting $\Delta\omega \leq \Delta\Omega/2$ into Eq. 2.3 gives

$$|\tau_1 - \tau_2| \leq 2A\Delta\Omega \tag{2.4}$$

$$|\tau_1 - \tau_2| \leq \frac{8\pi c A \Delta\Lambda}{\lambda_0^2} \tag{2.5}$$

For our experiment, $A = 2500\,\mathrm{fs}^2$, the acceptance bandwidth of our monochromator is $\Delta\Lambda = 0.35\,\mathrm{nm}$, and the central wavelength at which we apply the BARC-phase is $\lambda_0 = 809.6\,\mathrm{nm}$. With these parameters, one arrives at $|\tau_1 - \tau_2| \lesssim 10\,\mathrm{fs}$, corresponding to a $3\,\mu\mathrm{m}$ separation in motor position, or, when an index of refraction $n_{onion} = 1.3$ is assumed, an absolute separation of $2.3\,\mu\mathrm{m}$ between the sample layers. Hence, we only expect to see artifacts from interfaces closer than $2.3\,\mu\mathrm{m}$ inside the sample, which is below the resolution of our interferometer.

We see that while a suppression of artifacts is impossible in QOCT using state-of-the-art technology, it is comparatively easy to achieve in CPI using BARC pulses. It is interesting to note that artifact filtering in CPI only works when the pulse exhibits finite, or imperfect, frequency correlations. This is the experimentally relevant regime since, in practice, the correlation can never be perfect. In the limit $A \to \infty$, the frequency shift $\Delta\omega$ goes to zero, meaning that artifact features will essentially occur at the same frequency as the signal and the suppression of artifacts via spectral filtering will become unfeasible. The intermediate regime where A is large enough to cancel the effects of dispersion, yet small enough to allow a measurable spectral separation of artifacts from signal therefore

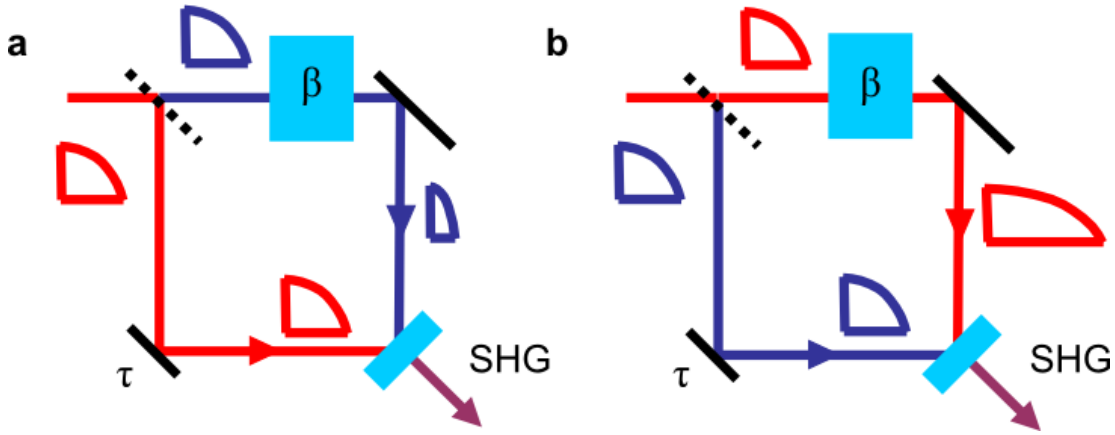

Figure 2.6: Cause of the dispersion-dependent frequency shift in CPI with the BARC-pulse. **a** and **b** depict the two interfering paths which lead to the CPI signal. The dispersive element compresses the blue half of the pulse for the paths in **a**, and lengthens the red half for the paths in **b**. In each case, the red half of the pulse is longer than the blue half when the pulses recombine on the nonlinear crystal. The net effect is that blue frequencies combine with slightly greater red frequencies than if there was no dispersion, leading to an overall blue shift in the signal.

proves to be ideally suited for our technique.

2.7.2 Wavelength shift in CPI with BARC-pulse

CPI using BARC-pulses exhibits a small dispersion-dependent wavelength shift that affects the central frequency and bandwidth of the SFG signal. The origin of the wavelength shift can be understood from the diagram shown in Figure 2.6.

The initial pulse is a superposition of a chirped "red" half of the pulse and an antichirped "blue" half. We assume that the pulses are in the large-chirp limit so that the red half has an instantaneous frequency $\omega_R(t) = \omega_0 + \frac{1}{2A}t$, for $-\infty < t \leq 0$, where A is a real, positive number; similarly the blue half has instantaneous frequency $\omega_B(t) = \omega_0 - \frac{1}{2A}t$, for $-\infty < t \leq 0$.

To illustrate this effect, Figure 2.6 depicts the two processes leading to narrow band

SFG from a single-interface sample. In Figure 2.6a, the antichirped blue half traverses the upper path while the chirped red half takes the lower; in Figure 2.6b, the roles are reversed. A purely quadratic dispersive element is located in the upper arm, which applies a frequency-dependent phase $\phi(\omega) = \beta(\omega - \omega_0)^2$, with β real and positive. We assume that $\beta \ll A$ so that the dispersion is small compared to the chirp parameter as is required for dispersion cancellation [24]. The effect of the material dispersion will further stretch a chirped pulse or compress an anti-chirped pulse.

We can determine the mean SFG frequency as a function of delay for the two amplitudes by simply adding the instantaneous frequencies for the two pulses in each of the cases shown in Figure 2.6. They are:

$$\omega_{SFG,a}(\tau) = 2\omega_0 - \frac{1}{2(A-\beta)}t + \frac{1}{2A}(t+\tau) \tag{2.6}$$

$$\omega_{SFG,b}(\tau) = 2\omega_0 + \frac{1}{2(A+\beta)}t - \frac{1}{2A}(t+\tau), \tag{2.7}$$

for the paths shown in Figures 2.6a and b respectively. We expect interference when the sum frequencies corresponding to these two paths are equal. Setting the two frequencies equal and solving for τ gives

$$\tau = \frac{t\beta^2}{(A-\beta)(A+\beta)}, \tag{2.8}$$

which leads to $\tau = 0$ to first order in β. Therefore, we expect interference when the interferometer paths are balanced as long as the additional dispersion is small. Substituting $\tau = 0$ into our expression for $\omega_{SFG,a}$ yields:

$$\omega_{SFG,a} = 2\omega_0 - \frac{1}{2(A-\beta)}t + \frac{1}{2A}t. \tag{2.9}$$

The last two terms constitute a frequency shift with respect to the expected $2\omega_0$. Calculating the shift to first order in β gives:

$$\Delta\omega = -\frac{t\beta}{2A^2}. \tag{2.10}$$

Because the dispersive element causes a small difference in the chirp rates of the two pulses, we expect a time-dependent shift in the SFG frequency. Note that such a frequency shift is not expected using the original method of CPI [13, 14], and the shift arises from the asymmetry of the BARC-pulses. Because the centre of the pulse is at some negative t, we expect a positive frequency shift.

We estimate the size of the shift in the following way. The electric field envelope of each half of the shaped pulse is modelled by a Gaussian $e^{-t^2/(2\sqrt{2}A\sigma_\omega)^2}$ for $t \leq 0$ (the field is 0 for $t > 0$), where σ_ω is the RMS frequency-bandwidth of the pulse's electric-field. When $\tau = 0$, these pulses overlap in the crystal (one from each interferometer arm), and the intensity of the SFG signal has approximately the temporal envelope $\left|e^{-t^2/(2A\sigma_\omega)^2}\right|^2$ for $t \leq 0$.

Half of our SFG signal is produced from light arriving before some time t_{avg}. The value for t_{avg} can be found as the solution to:

$$\int_{-\infty}^{t_{avg}} e^{-2t^2/(2A\sigma_\omega)^2} dt = \int_{t_{avg}}^{0} e^{-2t^2/(2A\sigma_\omega)^2} dt \tag{2.11}$$

which is $t_{avg} \approx -0.67A\sigma_\omega$. From this we estimate the frequency shift:

$$\Delta\omega \;=\; 0.34\frac{\beta\sigma_\omega}{2A} \tag{2.12}$$

In terms of the wavelength shift $\Delta\lambda$ that is:

$$\Delta\lambda \;=\; -0.17\frac{\beta\sigma_\lambda}{A}\left(\frac{\lambda_{signal}}{\lambda_{pulse}}\right)^2, \tag{2.13}$$

where λ_{signal} is the centre wavelength of the SFG signal when there is no unbalanced dispersion, λ_{pulse} is the centre wavelength of the BARC pulse, and σ_λ is the RMS frequency-bandwidth of the pulse's electric-field, in units of wavelength.

Assuming an input pulse centred at $\lambda_{pulse} = 809.60\,\text{nm}$ with 60 nm FWHM bandwidth (corresponding to our system acceptance bandwidth), a chirp parameter $A = 2500\,\text{fs}^2$, 3 mm BK7 in the sample arm ($\beta = 132\,\text{fs}^2$), and a signal wavelength $\lambda_{signal} = 403.80\,\text{nm}$

gives an expected wavelength shift of $\Delta\lambda = -0.2\,\mathrm{nm}$, explaining the small blue shift observed experimentally.

Chapter 3

Nonlinear chirping function for resolution improvement in CPI

3.1 Resolution disparity between CPI and QOCT

As shown in sections 1.3.1 and 1.3.2, the signal in a QOCT system is narrower than the CPI signal if the single-photon bandwidth of the source light is the same in both systems. For light sources with gaussian spectra, this difference is a factor of $\sqrt{2}$. The origin of this difference can perhaps best be understood by considering both systems in the limit of perfect frequency anticorrelations. The two-photon bandwidth function for an SPDC-produced two-photon state with perfect anticorrelations is (1.38) in the limit $\sigma_c \to \infty$:

$$f(\omega_1, \omega_2) = \exp\left[-\frac{(\omega_1 - \omega_0)^2}{8\sigma_{sp}^2}\right] \exp\left[-\frac{(\omega_2 - \omega_0)^2}{8\sigma_{sp}^2}\right] \delta(\omega_1 + \omega_2 - 2\omega_0) \tag{3.1}$$

Since this expression is for the high-correlation limit, the substitution $\sigma \to \sqrt{2}\sigma_{sp}$ has been made. The number of coincidence detection events as a function of time-delay is given by performing the ω_2 integral of (1.39):

$$C(\tau) \propto \int d\omega_1 e^{-\frac{(\omega_1 - \omega_0)^2}{2\sigma_{sp}^2}} \left[1 - \cos\left(2(\omega_1 - \omega_0)\tau\right)\right] \tag{3.2}$$

which can be evaluated to give a dip at $\tau = 0$ with width $1/2\sigma_{sp}$.

Now consider the system in Figure 2.1a which has two lasers of frequency $\omega_0 \pm \Delta$ as inputs to the interferometer at any one time. As shown in section 2.4.1 the SFG signal produced by such a frequency pair is given by $S(\Delta, \tau) = |E(\Delta)E(-\Delta)|^2 (1 + \cos[\phi_+(\Delta, \tau) - \phi_-(\Delta, \tau)])$ where $E(\Delta)$ is the electric field amplitude of the lasers. If all values of the offset Δ are swept over, the intensity of the measured signal will be:

$$I(\tau) = \int d\Delta \, |(E(\Delta)E(-\Delta)|^2 (1 + \cos(2\Delta(\alpha L - \tau))) \tag{3.3}$$

If the lasers have the same single-photon bandwidth as the QOCT system described above (i.e., $E(\Delta) = e^{-\Delta^2/4\sigma_{sp}^2}$) then (3.3) is

$$I(\tau) = \int d\Delta e^{-\frac{\Delta^2}{\sigma_{sp}^2}} (1 + \cos(2\Delta(\alpha L - \tau))) \tag{3.4}$$

This expression is almost identical to (3.2) except that the gaussian multiplying the cosine term is narrower by a factor of $\sqrt{2}$. This is precisely the factor by which the CPI signal is broader than the QOCT signal. The integrand in (3.3) is proportional to the square of the laser intensities; squaring a gaussian intensity function returns another gaussian which is narrower by a factor of $\sqrt{2}$. If the lasers had an intensity function which was constant in Δ, (i.e., if the bandwidth function had a "top-hat" profile, as opposed to a gaussian) squaring the intensities would return a bandwidth function with the same width. This would produce a CPI signal with a $\sqrt{2}$ resolution improvement [15].

3.1.1 Nonlinear chirp for narrower CPI signal

The above discussion made the argument that a source with a top-hat-shaped spectral bandwidth function would produce a CPI signal which is narrower in time than one with a gaussian spectral function. The source considered was a pair of monochromatic lasers with frequencies $\omega_0 \pm \Delta$ with a top-hat spectral function $E(\Delta)$. This source also has a *temporal* function with a top-hat shape if Δ is varied linearly in time. In this section we derive a nonlinear chirping function which will stretch a transform-limited gaussian pulse into one

which has a constant intensity along the length of the chirped pulse, and we simulate the expected width of a CPI signal produced with this function.

Consider a pulse with spectrum $I(\omega)$ which is chirped nonlinearly, i.e., the instantaneous pulse frequency $\omega(t)$ does not depend linearly on t. For the range of frequencies between ω and $\omega + \Delta\omega$ the pulse has been stretched by some factor $n(\omega)$, and as such the intensity at these frequencies has been decreased by this same factor. If it takes a time Δt for the frequency to change by $\Delta\omega$, then the relation $\Delta t/\Delta\omega \propto n(\omega)$ is true. If the ratio $I(\omega)/n(\omega)$ is constant the pulse will have a constant intensity in the time domain. Hence $n(\omega) \propto I(\omega)$, and in the limit where Δt and $\Delta\omega$ are infinitesimally small:

$$\frac{dt}{d\omega} = AI(\omega) \tag{3.5}$$

where A is a constant related to the total length of the chirped pulse. If the instantaneous pulse frequency increases montonically along the length of the pulse, rearranging the above and integrating gives:

$$t(\omega) = \int_0^t dt = A\int_{-\infty}^{\omega} I(\omega)d\omega \tag{3.6}$$

If the pulse spectrum is gaussian, and given by $I(\omega) = e^{-\frac{(\omega-\omega_0)^2}{2\sigma^2}}$, the right side of the equation becomes

$$t(\omega) = A\int_{-\infty}^{\omega} d\omega\, e^{-\frac{(\omega-\omega_0)^2}{2\sigma^2}} \tag{3.7}$$

$$= \frac{A}{2} + \frac{A}{\sqrt{2\pi\sigma^2}}\int_{\omega_0}^{\omega} d\omega\, e^{-\frac{(\omega-\omega_0)^2}{2\sigma^2}} \tag{3.8}$$

$$= \frac{A}{2} + \frac{A}{\sqrt{\pi}}\int_0^{\Omega} d\Omega\, e^{-\Omega^2} \tag{3.9}$$

$$= \frac{A}{2}\left(\mathrm{erf}\left(\frac{\omega-\omega_0}{\sqrt{2\sigma^2}}\right) + 1\right) \tag{3.10}$$

In the second step the constant A has been redefined such that $A\int_{-\infty}^{\omega_0} I(\omega)d\omega = A/2$, and in the third step the substitution $\Omega = (\omega-\omega_0)/\sqrt{2\sigma^2}$ is made. In the fourth step we apply the definition $\int_0^x e^{-x^2}dx = \mathrm{erf}(x)$. The phase $\phi(\omega)$ required to stretch a transform-limited

pulse into one with delays obeying the above expression for $t(\omega)$ can now be found by using the relation $\frac{d\phi}{d\omega} = t(\omega)$ [6]. If we make the simplifying assumption that the frequency element ω_0 will undergo no time-delay, we have:

$$\phi(\omega) = \int_{\omega_0}^{\omega} d\omega\, t(\omega) \tag{3.11}$$

Evaluating the above integral, and once again redefining A to absorb all multiplicitive constants gives:

$$\phi(\omega) = A\left[\frac{e^{-x^2}-1}{\sqrt{\pi}} + x\,\mathrm{erf}(x)\right]; \quad x = \frac{\omega-\omega_0}{\sqrt{2\sigma^2}} \tag{3.12}$$

This phase will stretch a transform-limited gaussian pulse centered at ω_0 with bandwidth σ into one which has an intensity which is constant in time. A superposition of two oppositely-chirped laser pulses will exhibit the required frequency anticorrelations needed for dispersion cancellation, and should give a CPI signal which is narrower than what would be obtained with linearly-chirped pulses.

A simulation was run to see the expected effects of the nonlinear chirp on the width of the CPI signal, and the results are in Figure 3.1. Three peaks were simulated, two with nonlinearly-chirped pulses and one with a linearly-chirped pulse. To represent the phase that could be applied in an experiment, a BARC-chirp was used, i.e., frequencies above the center frequency ω_0 were chirped with positive dispersion, and frequencies below ω_0 were antichirped with negative dispersion. The phase functions used in the simulation to apply the chirp were

$$\phi_{\mathrm{linear}}(\omega) = A_{lin.}(\omega-\omega_0)|\omega-\omega_0| \tag{3.13}$$

$$\phi_{\mathrm{nonlinear}}(\omega) = A_{nonlin.}\left[\frac{e^{-x^2}-1}{\sqrt{\pi}} + x\,\mathrm{erf}(x)\right]\frac{|x|}{x}; \quad x = \frac{\omega-\omega_0}{\sqrt{2\sigma^2}} \tag{3.14}$$

CPI signals from nonlinearly-chirped pulses with chirping parameters $A_{nonlin.} = 100$ and $A_{nonlin.} = 500$ were simulated. The signal from a linearly-chirped pulse with $A_{lin.} = 13,000\,\mathrm{fs}^2$ was also simulated. The parameter $A_{nonlin.} = 100$ was chosen as this is near the maximum nonlinear chirp that can be applied by the SLM. $A_{nonlin.} = 500$ was chosen

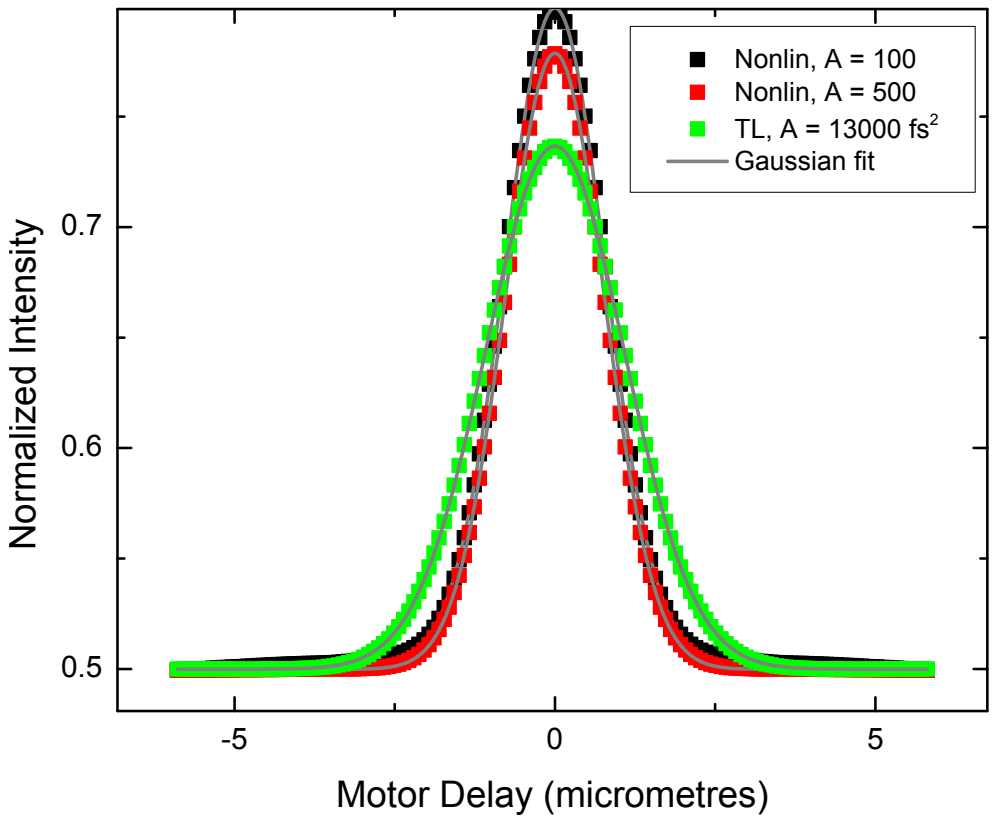

Figure 3.1: Simulation of CPI signal with nonlinearly- and linearly-chirped pulses. The red and black points represent the signal from nonlinearly-chirped pulses, and the green points are the signal from a linearly-chirped pulse. The peaks were normalized so their backgrounds were at a constant level of 0.5. The nonlinearly-chirped pulses have a narrower interference signal than the linearly-chirped pulse.

to see if stretching the pulse by a greater amount could further narrow the CPI signal, and $A_{lin.} = 13,000\,\text{fs}^2$ was chosen to create a chirped pulse with a similar length as the pulse with the stronger of the two nonlinear chirps. The simulated pulses had a centre frequency of 810 nm and a FWHM spectral bandwidth of 80 nm. The signal was simulated and filtered with a broad bandwidth of 50 nm so the background could be observed, and the filtered signals were normalized to have the same background level. The simulation did not include phase-matching, and the broadband second-harmonic-generation terms (i.e., the first two terms in (1.48)) are included in the filtered signal. This is why the background is approximately two-thirds of the peak heights. The filtered signals were fit with gaussian functions, and the nonlinearly-chirped-pulse peaks have widths of 1.84 μm and 1.82 μm. The narrower peak was the one with the higher chirping parameter. The linearly-chirped-pulse peak has a width of 2.56 μm, which is 39% and 41% broader than the nonlinearly-chirped-pulse peaks, respectively. The simulation suggests that chirping nonlinearly will narrow the CPI signal by a factor of $\sqrt{2}$.

3.1.2 Experimental test of nonlinear chirp

The experimental set-up in Figure 2.1b was used to compare the CPI signals produced with linearly- and nonlinearly-chirped pulses, as well as transform-limited pulses. In order to reduce the effects of phase-matching in the nonlinear crystal, a 0.1-mm piece of BBO was used for SFG, as opposed to the 0.5-mm piece used for the experiments in Chapter 2. The chirping functions applied to the SLM were those in (3.13) and (3.14).

The CPI signal was measured with a CCD camera in a spectrometer (Princeton Instruments PIXIS:2K in a Princeton Instruments Acton Advanced SP2750A) and integrated over a broad bandwidth to observe the constant background of the CPI signal (Figure 3.2). It is interesting to note that the background is not constant, but slowly decreases in intensity as the reference-arm mirror moves away from the location of the CPI peak. There is a simple reason for this discrepancy: as the mismatch between the interferometer arms increases, the upconverted light is at frequencies further away from $2\omega_0$. As the nonlinear crystal is aligned to optimize for SFG at $2\omega_0$, the SFG efficiency decreases as τ moves away from $\tau = 0$, and the height of the background decreases.

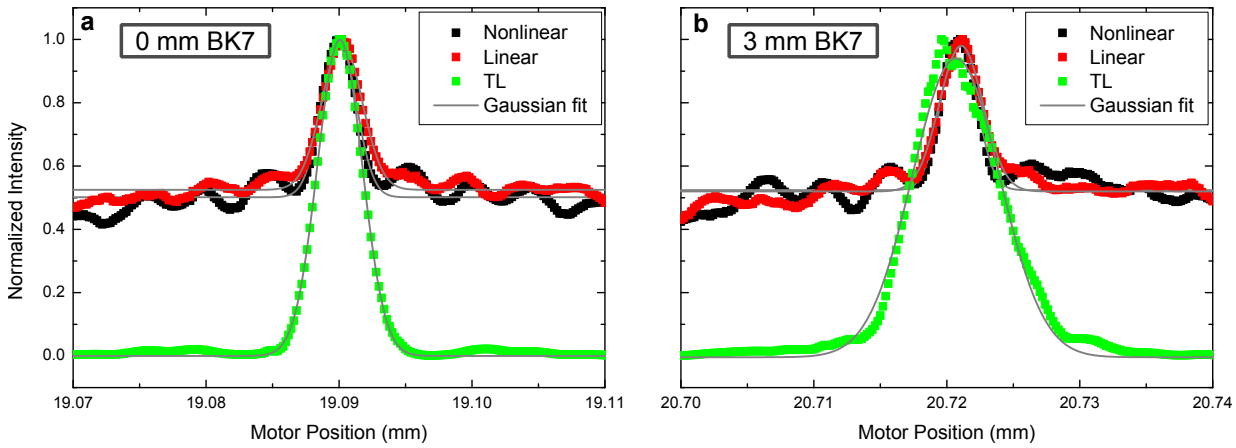

Figure 3.2: Comparison of CPI signals produced with linearly-chirped, nonlinearly-chirped, and transform-limited pulses. The SFG intensity was measured with a CCD camera and integrated over an 18 nm bandwidth. Since such a large intensity was integrated over, a background with approximately the same intensity as the CPI peak is seen when chirped pulses are used. The data in **a** was taken without any unbalanced quadratic dispersion in the interferometer, and the data in **b** was taken after a 3-mm-thick piece of BK7 glass was inserted into the sample arm. A constant background from the CCD camera was subtracted from each set of data, and the data were normalized to ease visual comparison of the peak widths. The black squares represent the data taken with nonlinearly-chirped pulses, red with linearly-chirped pulses, and green with transform-limited pulses. The grey lines are gaussian fits of the peaks. The nonlinearly-chirped pulses produce a narrower peak than the linearly-chirped and transform-limited pulses. Both chirped pulses exhibit dispersion-cancellation.

Chirping function	Peak FWHM (μm)	
	0 mm BK7	3 mm BK7
Nonlinear	3.0 ± 0.1	3.1 ± 0.1
Linear	3.6 ± 0.1	3.8 ± 0.1
None	3.95 ± 0.01	7.7 ± 0.1

Table 3.1: Widths of CPI signals from different chirping functions. The reported widths are the FWHM of the gaussian fits of the peaks in Figure 3.2. The reported errors are the standard error of the fits.

The data in Figure 3.2 show that the CPI signal produced by the nonlinearly chirped pulses is narrower than that produced by the linearly chirped ones. When there is no dispersion present, linearly-chirped pulses produce a 3.6-μm-wide peak which is 20% broader than the 3.0-μm-wide peak produced when the nonlinear chirp is used. When 3 mm of BK7 is added to one arm of the interferometer, both peaks exhibit dispersion cancellation. The linearly-chirped-pulse peak broadens by 6% to a width of 3.8 μm, and the nonlinearly-chirped-pulse peak broadens by 3% to 3.1 μm. In contrast, a peak produced with a transform-limited pulse broadens by over 90% (from 3.95 μm to 7.7 μm) when the BK7 is added. Hence the nonlinearly-pulses cancel dispersion just as effectively as the linearly-chirped ones.

The nonlinearly-chirped-pulse peaks are narrower than the linearly-chirped-pulse and transform-limited-pulse peaks, but not by the factor of $\sqrt{2}$ as predicted by the simulation. This could be due to the fact that the pulses do not have perfectly gaussian spectra. Another reason might be the pixelation of the SLM. Since the SLM is an array of liquid crystals, it does not apply a perfectly smooth chirping phase to the light passing through it. This can also partially explain the oscillations seen in the background, as simulations including the SLM pixelation showed this behaviour.

While the data in Figure 3.2 shows that the nonlinear chirping function will produce narrower peaks than the linear one, such a system can still produce artifacts if imaging

Chirping function	Peak FWHM (μm)	
	0 mm BK7	3 mm BK7
Nonlinear	3.97 ± 0.01	4.03 ± 0.02
Linear	4.71 ± 0.02	4.70 ± 0.01
None	3.56 ± 0.01	8.13 ± 0.03

Table 3.2: Widths of artifact-free CPI signals from different chirping functions. The reported widths are the FWHM of the gaussian fits of the peaks in Figure 3.3. The reported errors are the standard error of the fits.

samples with multiple layers. To ensure that no artifacts will be present in the CPI signal, the background must be completely filtered out. Figure 3.3 shows the same data as in Figure 3.2 where the background has been filtered out by only integrating the SFG intensity over a small bandwidth of 0.35 nm, centered on 405.46 nm. The CPI signal peaks have been fitted with gaussian functions, the widths of which are summarized in Table 3.1.2. While filtering out the background does increase the width of the CPI signal when either chirping function is used, the nonlinearly-chirped pulses still produce narrower peaks than the linearly-chirped ones. Both chirping functions cancel the quadratic dispersion introduced by the 3-mm-thick BK7 window.

The laser pulses used for this experiment had a FWHM bandwidth of 93 nm and were centered at 810 nm. The center chirp frequency ω_0 was set to correspond to the wavelength $\lambda_0 = 810.6\,\text{nm}$. The linear chirping function had the parameter $A_{lin.} = -3000\,\text{fs}^2$. The parameters for the nonlinear chirp were $A_{nonlin.} = -115$ and $\sigma_{FWHM} = 80\,\text{nm}$, where $\sigma_{FWHM} = 2\sqrt{2\ln(2)}\sigma$ is the full-width at half-maximum of a gaussian spectrum with bandwidth σ. The parameter $A_{nonlin.}$ was chosen to produce a pulse with a similar length in time as the linearly chirped one, then the bandwidth parameter σ was fine-tuned to minimize oscillations seen in the background of the CPI signal. The phase-matching of the SFG process is imperfect, and as a result, the *effective* bandwidth of the system is less than the laser bandwidth. This is a possible explanation for the discrepancy between the

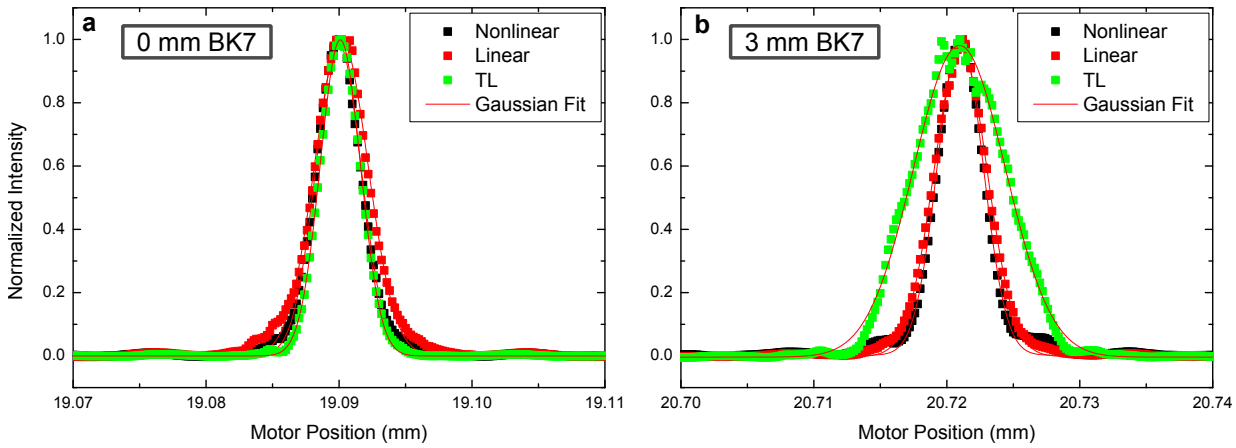

Figure 3.3: Comparison of artifact-free CPI signals produced with linearly-chirped, nonlinearly-chirped, and transform-limited pulses. The SFG intensity was measured with a CCD camera and integrated over a 0.35 nm bandwidth. The narrow filtering removes the background – and hence artifacts – from the signal. The data in **a** was taken without any unbalanced quadratic dispersion in the interferometer, and the data in **b** was taken after a 3-mm-thick piece of BK7 glass was inserted into the sample arm. A constant background from the CCD camera was subtracted from each set of data, and the data were normalized to ease visual comparison of the peak widths. The black squares represent the data taken with nonlinearly-chirped pulses, red with linearly-chirped pulses, and green with transform-limited pulses. The grey lines are gaussian fits of the peaks. Filtering the CPI signal slightly broadens the nonlinearly- and linearly-chirped-pulse peaks, although the nonlinear chirp still exhibits a resolution-advantage over the linear chirp. Both chirped pulses exhibit dispersion-cancellation.

measured laser bandwidth and the optimal bandwidth parameter for the nonlinear chirping function.

3.2 QOCT with imperfect frequency correlations and fast detectors

As explained in section 2.7.1, artifacts in the QOCT signal occur between every pair of sample interfaces. These artifacts are caused by interference between photon-coincidence-detection events resulting from photons which are reflected from different layers within the sample. In theory, artifacts can be filtered from the QOCT signal if the coincidence-detection window can be shorted to the tens-of-femtoseconds scale (although current technology limits coincidence windows to a few hundred picoseconds). To accurately compare QOCT to CPI, the following calculation determines the expected signal for a QOCT system which exhibits imperfect frequency correlations and uses detectors which are fast compared to the coherence time of the photons. The specific goal of this section is to see how the resolution and dispersion-cancelling properties of a QOCT system would be affected if artifacts could be filtered from the signal, or if a state with imperfect frequency correlations was used.

We will consider a modified QOCT setup with an extra beamsplitter before the detectors (Figure 3.4). When the path lengths of the interferometer are balanced photons will bunch at the first beamsplitter; if they are sent into mode $3'$ they are split at the second beamsplitter (the pair will travel through mode $4'$ with probability $1/2$, in which case both photons are lost and no coincidence events are counted). Hence, by placing one detector in each of modes 3 and 4, a coincidence peak will be observed, as opposed to a dip.

The two-photon state $|\psi_{1,2}\rangle$ produced from SPDC with a pump photon with frequency $2\omega_0$ is

$$|\psi_{1,2}\rangle = \int d\omega_1 d\omega_2 f(\omega_1, \omega_2)|\omega_1\rangle|\omega_2\rangle \tag{3.15}$$

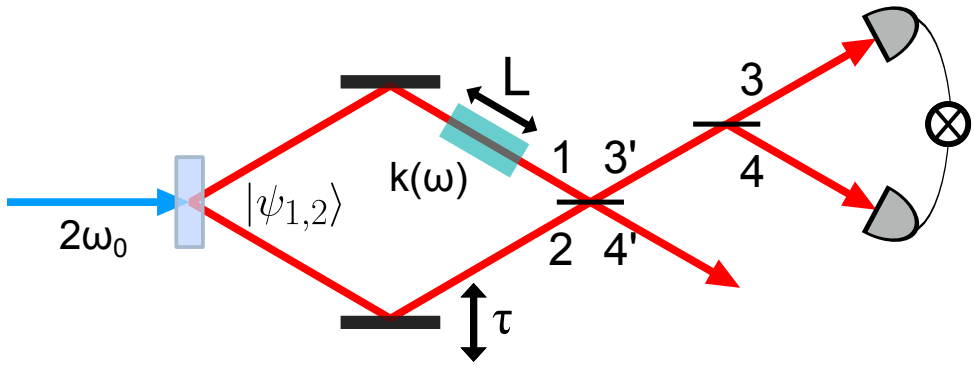

Figure 3.4: A set-up for producing a HOM peak. Photon pairs bunch into modes 3' and 4' at the first beamsplitter. A second beamsplitter in mode 3' splits bunched photons pairs into modes 3 and 4. The detectors in modes 3 and 4 register a coincidence *peak* as opposed to a dip when the interferometer arms are balanced.

where $f(\omega_1, \omega_2)$ is the two-photon joint spectrum, and is given by

$$f(\omega_1, \omega_2) = \exp\left[-\frac{(\omega_1 - \omega_0)^2}{4\sigma^2}\right] \exp\left[-\frac{(\omega_2 - \omega_0)^2}{4\sigma^2}\right] \exp\left[-\frac{(\omega_1 + \omega_2 - 2\omega_0)^2}{4\sigma_c^2}\right] \tag{3.16}$$

The parameter σ in the first two exponentials is related to the bandwidth of a single photon from the pair (which is more carefully defined in section 3.2.1 below), and σ_c is a measure of the strength of frequency correlation, which is related to the bandwidth of the pump photon. If $\sigma_c \ll \sigma$ the third exponential becomes very narrow and the relation $\omega_1 + \omega_2 = 2\omega_0$ is enforced. In the other limit where $\sigma_c \gg \sigma$, the photons become completely uncorrelated in frequency.

To obtain an expression for the number of coincidence-detection events we first define the joint probability $P_{3,4}(t_1, t_2)$ of one photon being in each of modes 3 and 4 at times t_1 and t_2, respectively [28]

$$P_{3,4}(t_1, t_2, \tau, \epsilon) \propto \langle E_3^-(t_1) E_4^-(t_2) E_3^+(t_1) E_4^+(t_2) \rangle \tag{3.17}$$

where $E_i^{\pm}(t) \propto \int d\omega_i \sqrt{\omega_i} \hat{a}_i^{\mp}(\omega_i) e^{\mp \omega_i t}$ are the forwards and backwards propagating electric

field operators for the i-th mode, and $\hat{a}_i^-(\omega)$ and $\hat{a}_i^+(\omega)$ are the respective annhilation and creation operators for photons in mode i and with frequency ω [28]. The τ and ϵ dependence is presently hidden in the creation and annhilation operators for modes 3 and 4 which will pick up phases dependent on both τ and ϵ as the state $|\psi_{1,2}\rangle$ is propagated through the interferometer to the detectors. The window for coincidence detection can be modelled by a function $g(t_1 - t_2)$ which depends on only the difference in arrival times of the photons at each detector; the function is peaked when $t_1 - t_2 = 0$, and it decays to zero on either side of this peak. The total number of recorded coincidences $C(\tau, \epsilon)$ is found by integrating the coincidence-window-modulated joint-probability distribution over all times t_1 and t_2 [28]:

$$C(\tau, \epsilon) \propto \iint dt_1 dt_2 \, g(t_1 - t_2) P_{3,4}(t_1, t_2, \tau, \epsilon) \tag{3.18}$$

To evaluate the joint-probability function $P_{3,4}(t_1, t_2, \tau, \epsilon)$, the state $|\psi_{1,2}\rangle$ is propagated through the interferometer from the source to the detectors. The dispersive element in mode 1 contributes a quadratic phase of $\phi_1(\omega) = \epsilon(\omega - \omega_0)^2$ and the time-delay τ in mode 2 is represented by the phase $\phi_2(\omega) = -\omega_2 \tau$. Hence, immediately before the first beamsplitter, the state is:

$$|\psi_{1,2}\rangle = \int d\omega_1 d\omega_2 \, f(\omega_1, \omega_2) e^{i\phi_1(\omega_1) - i\phi_2(\omega_2)} \hat{a}_1^+(\omega_1) \hat{a}_2^+(\omega_2) |0\rangle_1 |0\rangle_2 \tag{3.19}$$

At the first beamsplitter, the creation operators are transformed as

$$\hat{a}_1^+(\omega) \to \frac{1}{\sqrt{2}} \left[\hat{a}_{3'}^+(\omega_1) + \hat{a}_{4'}^+(\omega_1) \right] \tag{3.20}$$

$$\hat{a}_2^+(\omega) \to \frac{1}{\sqrt{2}} \left[\hat{a}_{3'}^+(\omega_1) - \hat{a}_{4'}^+(\omega_1) \right] \tag{3.21}$$

Coincidences are only measured when both photons travel through mode $3'$ to the second beamsplitter, hence we drop the $\hat{a}_{4'}^+(\omega_i)$ terms and, making the second transformation

$\hat{a}^+_{3'}(\omega) \to \frac{1}{\sqrt{2}}\left[\hat{a}^+_3(\omega_1) - \hat{a}^+_4(\omega_1)\right]$, we have

$$|\psi_{3,4}\rangle = \frac{1}{4}\iint d\omega_1 d\omega_2 e^{i\epsilon(\omega_1-\omega_0)^2} e^{-i\omega_2\tau} f(\omega_1,\omega_2)\left[\hat{a}^+_3(\omega_1) - \hat{a}^+_4(\omega_1)\right]\left[\hat{a}^+_3(\omega_2) - \hat{a}^+_4(\omega_2)\right]|0\rangle_3|0\rangle_4 \tag{3.22}$$

We are now ready to evaluate the joint probability function. Absorbing the $\sqrt{\omega_i}$ terms into the two-photon bandwidth function gives:

$$P_{3,4}(t_1,t_2,\tau,\epsilon) \propto \iiiint d\omega_{3'} d\omega_{4'} d\omega_3 d\omega_4 \langle\psi_{3,4}|a^+_3(\omega'_3)a^+_4(\omega'_4)a^-_3(\omega_3)a^-_4(\omega_4)|\psi_{3,4}\rangle \tag{3.23}$$

$$= \sum_{n=0}^{\infty} \iiiint d\omega_{3'} d\omega_{4'} d\omega_3 d\omega_4 \langle\psi_{3,4}|a^+_3(\omega'_3)a^+_4(\omega'_4)|n\rangle\langle n|a^-_3(\omega_3)a^-_4(\omega_4)|\psi_{3,4}\rangle \tag{3.24}$$

$$= \left|\iint d\omega_3 d\omega_4 \langle 0|a^-_3(\omega_3)a^-_4(\omega_4)|\psi_{3,4}\rangle\right|^2 \tag{3.25}$$

where the identity is inserted in the second step and the last step follows from the fact that $|\psi_{3,4}\rangle$ contains no more than one photon in each of modes 3 and 4. Since annihilating one photon from each mode can only leave the vacuum state, the $n \neq 0$ terms can be dropped from the sum [28].

The matrix element in (3.25) is evaluated by inserting the explicit expression for $|\psi_{3,4}\rangle$

$$\begin{aligned}\langle 0|a^-_3(\omega_3)a^-_4(\omega_4)|\psi_{3,4}\rangle = \iint d\omega_1 d\omega_2 \Big\{ &\langle 0|a^-_3(\omega_3)a^-_4(\omega_4) f(\omega_1,\omega_2) e^{i\phi_1(\omega_1)-i\phi_2(\omega_2)} \\ &\times \left[\hat{a}^+_3(\omega_1) - \hat{a}^+_4(\omega_1)\right]\left[\hat{a}^+_3(\omega_2) - \hat{a}^+_4(\omega_2)\right]|0\rangle_3|0\rangle_4 \Big\}\end{aligned} \tag{3.26}$$

$$= -f(\omega_3,\omega_4)\left[e^{i\phi_1(\omega_3)-i\phi_2(\omega_4)} + e^{i\phi_1(\omega_4)-i\phi_2(\omega_3)}\right] \tag{3.27}$$

where in the second step we invoke the symmetry of the two-photon bandwidth function $f(\omega_1,\omega_2) = f(\omega_2,\omega_1)$. Finally we are ready to evaluate (3.18), which has now become:

$$C(\tau,\epsilon) \propto \iint dt_1 dt_2 e^{-\frac{(t_1-t_2)^2}{2\sigma_t^2}} \left|\iint d\omega_3 d\omega_4 f(\omega_3,\omega_4)\left[e^{i\phi_1(\omega_3)-i\phi_2(\omega_4)} + e^{i\phi_1(\omega_4)-i\phi_2(\omega_3)}\right]\right|^2 \tag{3.28}$$

If we use $g(t_1, t_2) = e^{-\frac{(t_1-t_2)^2}{2\sigma_t^2}}$ for the coincidence gating function, evaluating the above gives:

$$C(\tau, \epsilon) \propto A_1 e^{-\frac{\tau}{2\tau_1^2}} + A_2 e^{-\frac{\tau}{2\tau_2^2}} \tag{3.29}$$

where

$$A_1 = \sqrt{\frac{1}{\sigma_c^2 + 2\sigma^2\left[1 + 4\epsilon^2\sigma^2(\sigma^2 + \sigma_c^2) + (2\sigma^2 + \sigma_c^2)\sigma_t^2\right]}} \tag{3.30}$$

$$A_2 = \sqrt{\frac{1}{\sigma_c^2 + 2\sigma^2\left[1 + 4\epsilon^2\sigma^2(\sigma^2(1 + \sigma_c^2\sigma_t^2) + \sigma_c^2) + (2\sigma^2 + \sigma_c^2)\sigma_t^2\right]}} \tag{3.31}$$

$$\tau_1 = \sqrt{\frac{1}{2\sigma^2} + 4\epsilon^2\sigma^2\left(1 - \frac{1}{2\sigma^2 + \sigma_c^2}\right) + \sigma_t^2} \tag{3.32}$$

$$\tau_2 = \sqrt{\frac{2\sigma^2 + \sigma_c^2 + 4\epsilon^2\sigma^4\sigma_c^2}{4\sigma^4 + 2\sigma^2\sigma_c^2} + \frac{2\epsilon^2\sigma^2}{1 + 2\sigma^2\sigma_t^2}} \tag{3.33}$$

3.2.1 Definition of "single-photon bandwidth" in QOCT

To compare the resolutions of different imaging techniques fairly, each system must have a well-defined single-photon bandwidth. After this bandwidth is set, different systems with the same single-photon bandwidths can be fairly compared. For WLI and CPI systems it is straightforward to read the single-photon bandwidth directly from the spectral function of the source light. This is not so simple with QOCT, however. The joint-spectrum $f(\omega_1, \omega_2)$ (1.38) used in the definition of the two-photon state used for QOCT does not clearly indicate the bandwidth of each photon independently. In the section below we define the single-photon bandwidth of a two-photon state, and relate it to the parameters σ and σ_c in the expression for the joint-spectrum.

Experimentally, the single photon bandwidth of a two-photon state can be measured by taking one photon and measuring its bandwidth with a spectrometer. This is represented mathematically by tracing out one of the photons in the two-photon state and calculating the intensity of the remaining photon as a function of frequency.

The density matrix of a pair of photons generated by SPDC is written as

$$\rho_{1,2} = \int d\omega_1' d\omega_2' d\omega_1 d\omega_2 f^*(\omega_1', \omega_2') f(\omega_1, \omega_2) |\omega_1\rangle |\omega_2\rangle \langle\omega_1'| \langle\omega_2'| \tag{3.34}$$

where $f(\omega_1, \omega_2)$ is the two-photon joint-spectrum and the * denotes the complex conjugate. After tracing out photon two, the state, ρ_1 of the remaining photon is:

$$\begin{aligned}
\rho_1 &= Tr_2(\rho_{1,2}) && (3.35)\\
&= \int d\omega_2'' \langle\omega_2''|\rho_{1,2}|\omega_2''\rangle && (3.36)\\
&= \int d\omega_2'' \int d\omega_1' d\omega_2' d\omega_1 d\omega_2 f^*(\omega_1', \omega_2') f(\omega_1, \omega_2) |\omega_1\rangle \langle\omega_1'| \delta(\omega_2 - \omega_2'') \delta(\omega_2' - \omega_2'') && (3.37)\\
&= \int d\omega_2'' \int d\omega_1' d\omega_1 f^*(\omega_1', \omega_2'') f(\omega_1, \omega_2'') |\omega_1\rangle \langle\omega_1'| && (3.38)\\
&= \int d\omega_1 d\omega_1' F(\omega_1, \omega_1') |\omega_1\rangle \langle\omega_1'| && (3.39)
\end{aligned}$$

The resulting spectrum of the single-photon is found by measuring the expectation value of the number operator $\hat{n} = \hat{a}^\dagger \hat{a}$ as a function of frequency.

$$\begin{aligned}
I(\omega) &\propto \langle \hat{n}(\omega) \rangle && (3.40)\\
&= Tr(\hat{a}^\dagger(\omega) \hat{a}(\omega) \rho_1) && (3.41)\\
&= F(\omega) && (3.42)
\end{aligned}$$

where $F(\omega)$ is the same function appearing in Eq. 3.39 evaluated at $\omega_1 = \omega_1' = \omega$. Hence $F(\omega)$ is the single-photon spectrum of photon one. Using the assumption that the original two-photon state has a frequency correlation function

$$f(\omega_1, \omega_2) = \exp\left[-\frac{(\omega_1 - \omega_0)^2}{4\sigma^2}\right] \exp\left[-\frac{(\omega_2 - \omega_0)^2}{4\sigma^2}\right] \exp\left[-\frac{(\omega_1 + \omega_2 - 2\omega_0)^2}{4\sigma_c^2}\right] \tag{3.43}$$

gives the single-photon intensity spectrum $F(\omega) = e^{-\frac{-(\omega_1 - \omega_0)^2}{2} \frac{(2\sigma^2 + \sigma_c^2)}{\sigma^2(\sigma^2 + \sigma_c^2)}}$. The single-photon

bandwidth, σ_{sp}, can be read off from this equation to give

$$\sigma_{sp}^2 = \sigma^2 \frac{\sigma^2 + \sigma_c^2}{2\sigma^2 + \sigma_c^2} \tag{3.44}$$

We see that the single-photon bandwidth is affected by the strength of correlations between the two photons. If the two photons are uncorrelated in frequency (i.e., $\sigma_c \gg \sigma$) we have $\sigma_{sp} = \sigma$. In the opposite case, in the limit of perfect correlation between the two photons' frequencies, (i.e., $\sigma_c \ll \sigma$), we see that $\sigma_{sp} \to \sigma/\sqrt{2}$. In this case, tracing out photon two gives a narrower bandwidth for photon one.

Now a direct comparison can be made between QOCT systems which exhibit different two-photon correlation strengths. By ensuring the *single-photon* bandwidth is constant, the effect of the correlation strength on the resolution of a QOCT system can be seen.

3.2.2 Four interesting limits and comparison to CPI

Now that we have an analytical expression for the measured coincidences as a function of the time-delay, we can examine the signal's properties in the limits where infinitely fast or slow detectors are used, and when the photon pairs are perfectly frequency anticorrelated or completely uncorrelated. The widths of the two gaussians in (3.29) are related to τ_1 and τ_2, and their values in the above mentioned limits are summarized in Table 3.3.

The first row of the table is the limit of perfect correlations and slow detectors, which gives a constant background with a peak of width $1/2\sigma_{sp}$. If slow detectors are still used and a state with no frequency correlations is chosen (second row of the table), the signal is still a peak rising from a constant background, but the width and visibility of the peak are now sensitive to dispersion. When photon pairs with completely uncorrelated frequencies are used the minimum signal width broadens to $1/\sqrt{2}\sigma_{sp}$. These two results are what one would obtain by taking the corresponding limits of (1.42), which was derived with the assumption that the detectors are very slow.

The bottom two rows of Table 3.3 are the limits of using infinitely fast detectors. In this limit the constant background is completely filtered out of the signal, and the two Gaussian

Situation	τ_1	τ_2	A_2/A_1
$\sigma_c \to 0$, $\sigma_t \to \infty$	∞	$\frac{1}{2\sigma_{sp}}$	1
$\sigma_c \to \infty$, $\sigma_t \to \infty$	∞	$\frac{1}{\sqrt{2}\sigma_{sp}}\sqrt{1+4\epsilon^2\sigma_{sp}^4}$	$\sqrt{\frac{1}{1+4\epsilon^2\sigma_{sp}^4}}$
$\sigma_c \to 0$, $\sigma_t \to 0$	$\frac{1}{2\sigma_{sp}}\sqrt{1+16\epsilon^2\sigma_{sp}^4}$	$\frac{1}{2\sigma_{sp}}\sqrt{1+16\epsilon^2\sigma_{sp}^4}$	1
$\sigma_c \to \infty$, $\sigma_t \to 0$	$\frac{1}{\sqrt{2}\sigma_{sp}}\sqrt{1+8\epsilon^2\sigma_{sp}^4}$	$\frac{1}{\sqrt{2}\sigma_{sp}}\sqrt{1+8\epsilon^2\sigma_{sp}^4}$	1

Table 3.3: Characteristics of the QOCT signal with imperfect frequency correlations and artifact filtering. The temporal widths of the two gaussians which make up the QOCT signal in (3.29) are given in the limits of infinitely short and long coincidence detection windows for two-photon states which exhibit perfect frequency anticorrelations and no frequency correlations. The third column gives the ratio of the amplitudes of the two Gaussians. In the two cases where $\tau_1 \to \infty$, this ratio relates to the visibility of the peak rising from the constant background.

terms in (3.29) become identical. This reason the background is filtered out of the signal is because infinitely fast detectors can only register coincidences if the two photons arrive at the detectors at the same time, which can only happen when the interferometer arms are balanced, or when $\tau = 0$. The signal is now a single Gaussian peak with a dispersion-dependent width. The signal from perfectly-anticorrelated photon pairs has a minimum width $1/2\sigma_{sp}$ compared to $1/\sqrt{2}\sigma_{sp}$ for the signal from completely uncorrelated photon pairs.

The behaviour of the QOCT and CPI signals are similar when very high frequency-correlations are present. If artifacts are not filtered out, both signals will perfectly cancel dispersion. When the nonlinear chirping function is used in CPI, both signals will have a width of $1/2\sigma$. If the artifacts are filtered from the QOCT signal by using infinitely-fast detectors, the signal is no longer dispersion-cancelling, but it has the same minimum width. It is interesting to note that in CPI the artifact-free signal has a minimum width of $1/\sqrt{2}\sigma$.

The reason for this broadening can be seen by examining the expression for the SFG-

field amplitude given by

$$E_{signal}(\omega,\tau) \approx \int d\omega' \left[E_-(\omega')E_+(\omega-\omega') - E_+(\omega')E_-(\omega-\omega')\right] e^{i\epsilon(\omega'-\omega_0)^2} e^{i(\omega-\omega')\tau} \quad (3.45)$$

where the field terms $E_\pm(\omega)$ are the positively- and negatively-chirped pulses:

$$E_\pm(\omega) \propto e^{-\frac{(\omega-\omega_0)^2}{4\sigma^2}} e^{\pm i\phi_{chirp}(\omega)} \quad (3.46)$$

The effect of filtering the SFG field narrowly around $2\omega_0$ can be seen by evaluating (3.45) at $2\omega_0$. If the phase ϕ_{chirp} is the nonlinear chirp defined in (3.12) the chirping terms will cancel each other out and the signal is given by

$$E_{signal}(2\omega_0,\tau) \approx \int d\omega' \, e^{-\frac{(\omega'-\omega_0)^2}{2\sigma^2}} e^{i\epsilon(\omega'-\omega_0)^2} e^{i(2\omega_0-\omega')\tau} \quad (3.47)$$

The chirp has no effect on the SFG light at $2\omega_0$, and hence cannot affect the width of the CPI signal. Interestingly, the same reasoning can be applied to see why the CPI signal does not cancel dispersion as effectively if it is filtered very narrowly.

Chapter 4

Signal improvement to CPI

One step towards increasing the power of the CPI signal is to improve the efficiency of the SFG process. A method of accomplishing this is to use a longer nonlinear crystal (which still allows phase-matching over the bandwidth of the source light) so the interaction time between beams from each interferometer arm is larger [4]. However, using a longer crystal will also increase the amount of background light, namely the narrowband SFG light created from the sum of the chirped and antichirped components coming from the same interferometer arm. Since this light is in a different spatial mode than the CPI signal, it is normally filtered spatially. However, if a longer nonlinear crystal is used the noncollinear angle between the two beams inside the crystal will have to be decreased, reducing the effectiveness of this spatial filtering. Furthermore, the longer nonlinear crystal will increase the intensity of the background and signal SFG light by similar amounts. Hence, while increasing the length of the nonlinear crystal used in a CPI set-up will increase the total intensity of the CPI signal light, it may also have the undesirable effect of increasing the measured background by a larger amount.

4.1 Offset-CPI

The above discussion assumes that both arms of the interferometer contain pulses which are chirped about the same center frequency. For example, if this center frequency was

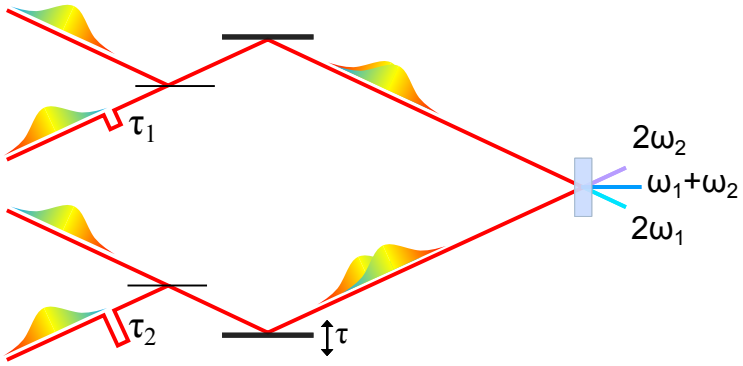

Figure 4.1: CPI set-up with spectrally separated signal and background. The sample and reference arms of the interferometer contain superpositions of a chirped and an antichirped pulse. The pulses are superposed with a delay between their ω_0 frequency components of τ_1 and τ_2 so they have average frequencies ω_1 and ω_2 for the sample and reference arms, respectively. The CPI signal is at a frequency $\omega_1 + \omega_2$, while the narrowband components of the background is at frequencies $2\omega_1$ and $2\omega_2$.

ω_0, both the background and signal would be at frequency $2\omega_0$. If the light in both arms was chirped about different center frequencies, say ω_1 and ω_2, then the signal would be at frequency $\omega_1 + \omega_2$, and the background light from both interferometer arms would be at the frequencies $2\omega_1$ and $2\omega_2$. With such a set-up, spectral filtering could be used in conjunction with spatial filtering to remove the background from the signal. We call such a system an offset-CPI (OCPI) system.

A hypothetical OCPI set-up is shown in Figure 4.1. Each arm of the interferometer contains a superposition of a chirped and an antichirped pulse where the ω_0 frequency component of the antichirped pulse is delayed relative to the ω_0 component of the chirped pulse. For the sample and reference arms these delays are τ_1 and τ_2, respectively. These time delays move the center frequency of each superposition away from ω_0 and if the difference between τ_1 and τ_2 is large enough, the narrowband component of the background can be easily separated from the OCPI signal with a spectrometer.

The electric fields in the sample and reference arms are $E_1(\omega)$ and $E_2(\omega)$, respectively,

given by:

$$E_1(\omega) = \left[E_+(\omega) + E_-(\omega)e^{i\omega\tau_1}\right] e^{i\epsilon(\omega-\omega_0)^2} \tag{4.1}$$

$$E_2(\omega) = \left[E_+(\omega) + E_-(\omega)e^{i\omega\tau_2}\right] e^{i\omega\tau} \tag{4.2}$$

where ϵ is the amount of unbalanced quadratic dispersion present in the sample arm, τ is the time-delay introduced by the moveable mirror in the reference arm, and $E_\pm(\omega) = \mathcal{E}e^{-\frac{(\omega-\omega_0)^2}{4\sigma^2}}e^{i\phi_\pm(\omega)}$ are the fields of the chirped and antichirped pulses. The electric field $E_{signal}(\omega)$ of the OCPI signal is the convolution of E_1 and E_2. Dropping the terms leading to broadband SFG (as done in (1.49)) gives:

$$E_{signal}(\omega) \approx \int d\omega' \left[E_-(\omega)E_+(\omega-\omega') + E_+(\omega)E_-(\omega-\omega')\right] e^{i\epsilon(\omega'-\omega_0)^2} e^{i(\omega-\omega')\tau} \tag{4.3}$$

The total CPI signal can be found by integrating the intensity of the SFG field over all frequencies, i.e., $I_{signal}(\tau) = \int |E_{signal}(\omega)|^2 \, d\omega$. Evaluating this integral and taking the large-chirp limit where both conditions $A\sigma^2 \gg 1$ and $A/\epsilon \gg 1$ are satisfied gives the following:

$$I_{signal}(\tau) \propto 1 + \cos\left(\omega_0(\tau_1 - \tau_2)\right) e^{-\left(\tau - \frac{\tau_1+\tau_2}{2}\right)^2\sigma^2} \tag{4.4}$$

This signal has a similar form to the CPI signal in (1.51). The OCPI signal is formed from a constant background with a gaussion of width $\Delta\tau = 1/\sqrt{2}\sigma$ added to it. The gaussian is multiplied by the phase-dependent term $\cos\left(\omega_0(\tau_1 - \tau_2)\right)$, however, which determines if the interference in the interferometer is constructive, destructive, or somewhere in-between. The argument of the cosine is the time-delay difference $(\tau_1 - \tau_2)$ multiplied by the center pulse frequency ω_0, so in order to produce a measurable signal an OCPI set-up must introduce the time-delays in a way that is stable on the order of the laser wavelength.

A proposal for an OCPI set-up with the required stability is seen in Figure 4.2. A laser pulse is split and each half is chirped with either positive or negative dispersion. The pulse polarizations are rotated to 45° and the antichirped pulse travels through a birefringent crystal which delays the vertical component of the pulse, but not the horizontal one. Introducing the time delays τ_1 and τ_2 in this way is stable because fluctuations in the crystal's position will affect both time delays equally, and hence not affect their difference.

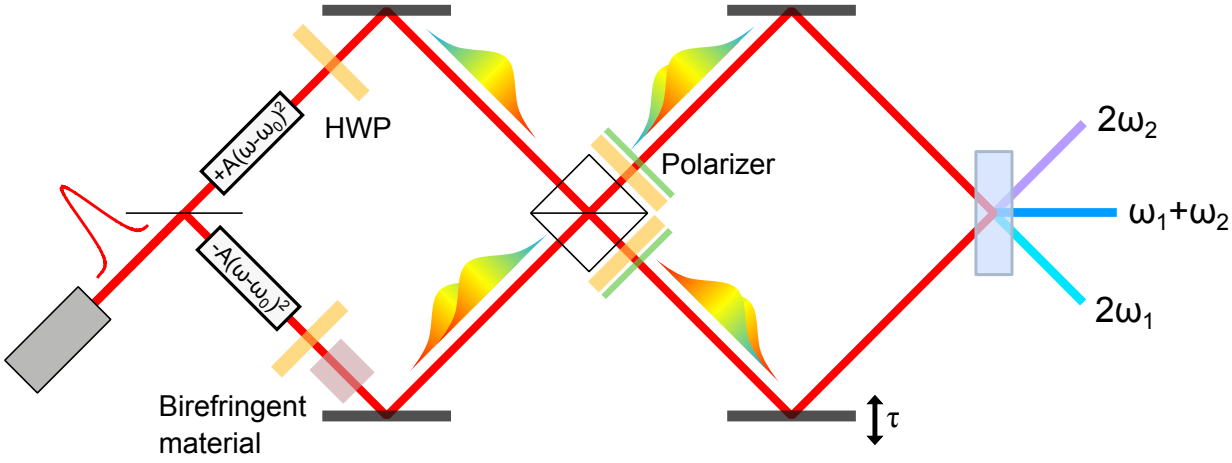

Figure 4.2: OCPI set-up with stable time-delay difference. A horizontally-polarized pulse is split on a 50:50 beamsplitter, one half is chirped with positive dispersion and the other is antichirped with an equal but opposite amount of negative dispersion. Both pulse polarizations are rotated by 45° by half-wave plates, and the vertically-polarized component of the antichirped pulse is delayed relative to the horizontally-polarized component by a birefringent material. The pulses are then combined on a polarizing beamsplitter and sent into the interferometer. The polarization in each interferometer arm is once again rotated by 45° and then sent through a horizontal polarizer. The light then travels through the interferometer and is recombined on a nonlinear crystal where it undergoes SFG.

If the chirped and antichirped beams are then recombined on a polarizing beam-splitter the outputs of the beamsplitter will contain superpositions of chirped and antichirped pulses with different centre frequencies.

The magnitude of the separation of the narrowband background and the signal is found by first remembering that the instantaneous frequency of a chirped pulse follows the function $\omega(t) = \omega_0 + t/2A$. If a chirped pulse with no time-delay is superposed with an antichirped pulse which has been delayed by a time τ the average frequency of the superposition will be

$$\omega_{avg}(t) = \frac{1}{2}\left[\left(\omega_0 + \frac{t}{2A}\right) + \left(\omega_0 + \frac{t-\tau}{2(-A)}\right)\right] = \omega_0 + \frac{\tau}{2A} \tag{4.5}$$

Delaying the antichirped pulse relative to the chirped pulse by a time τ increases the average frequency of the superposition. The narrowband component of the SFG light created by upconverting this pulse will be at a frequency $2\omega_0 + \tau/A$.

4.1.1 Simulation of OCPI

A simulation was performed to investigate the properties of an OCPI signal. 90 nm FWHM bandwidth pulses centred around 810 nm were used in the simulation. The linear chirping functions $\phi_\pm(\omega) = \pm A(\omega - \omega_0)^2$ with $A = 50,000\,\text{fs}^2$ were used. The pulses in the sample arm of the interferometer were combined with a time delay $\tau_1 = -251\,\text{fs}$, and the pulses in the reference were combined with a delay $\tau_2 = 251\,\text{fs}$. Both the narrowband and broadband background components of the SFG light created from the pulse in the reference arm were included in the simulation. The background from the sample-arm pulse was not included, as this typically has a very small intensity for samples with low reflectivity. The simulated OCPI signal was measured at 405 nm with a bandwidth of 0.05 nm. The narrowband component of the background was at 404.8 nm and was thus successfully filtered out of the OCPI signal. The simulation was run twice, with $0\,\text{fs}^2$ and $150\,\text{fs}^2$ of unbalanced dispersion present in the sample arm. For comparison, the signal produced with transform-limited pulses was simulated as well. The background light from the reference arm was not included in the simulation using the transform-limited pulses. The results of the simulation are in Figure 4.3.

The peaks from the simulation were fit with gaussians, and the FWHM of these gaussians were used to determine the widths of the peaks. The OCPI peak broadens from $6.5 \pm 0.1\,\mu\text{m}$ to $7.9 \pm 0.1\,\mu\text{m}$ when the quadratic dispersion is included in the simulation. The peak from the transform-limited pulse broadens from $2.3\,\mu\text{m}$ to $8.5\,\mu\text{m}$. The reported errors are the standard errors in the fits; the fits of the transform-limited-pulse peaks had standard errors for the FWHM on the order of $10^{-10}\,\mu\text{m}$. The simulation shows that filtering artifacts from the OCPI signal broadens it in relation to the transform-limited-pulse peak, however, in the presence of dispersion, OCPI can give a narrower signal than the transform-limited pulses.

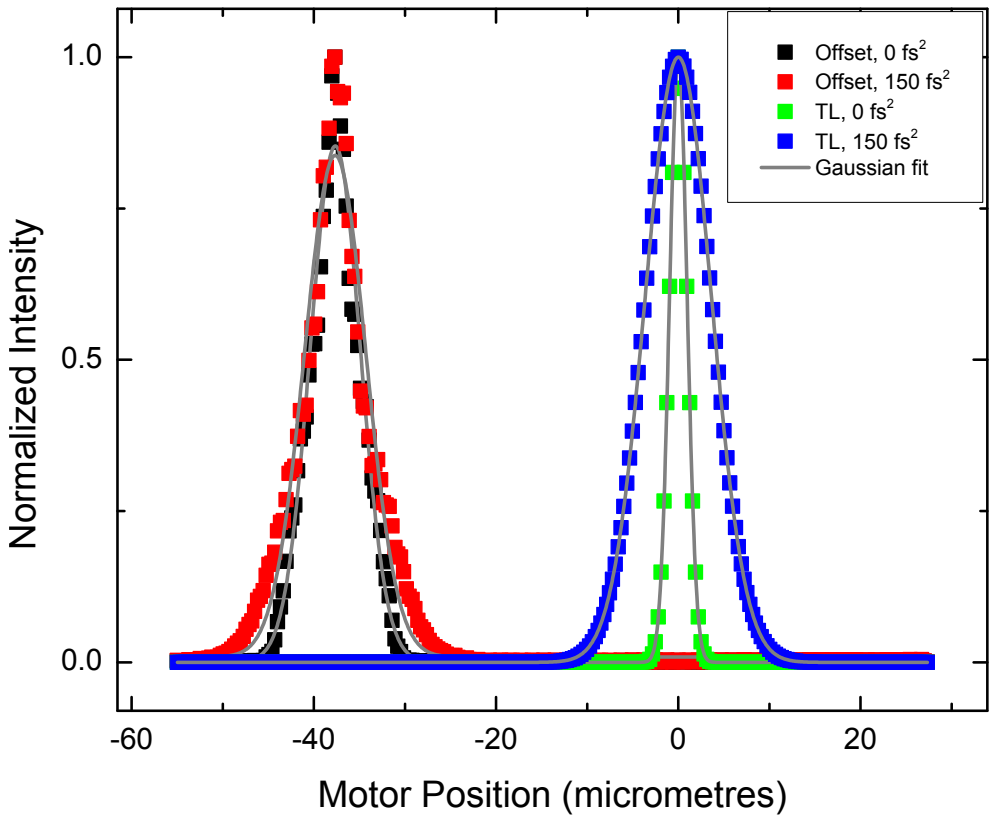

Figure 4.3: Simulated OCPI signal. The red and black squares are the simulated OCPI signal with $0\,\mathrm{fs}^2$ and $150\,\mathrm{fs}^2$ of unbalanced quadratic dispersion, respectively. The antichirped pulse was delayed relative to the chirped pulse in the sample and reference arms by $-251\,\mathrm{fs}$ and $251\,\mathrm{fs}$, respectively. The green and blue squares are the signal from transform-limited pulses, with and without unbalanced quadratic dispersion. The peaks were normalized to aid visual comparison of their widths.

4.1.2 Implementation of linear chirp

One way to linearly chirp a pulse with negative quadratic dispersion is to use a grating-based compressor (Figure 4.4). A grating compressor consists of two parallel gratings separated by a distance b, and a mirror. A light pulse is incident on the first grating at an angle β from normal incidence, and the different frequency components of the pulse are diffracted at an angle β' given by the grating equation (1.23). The grooves of the grating are separated by a distance d. The dispersed light hits a second grating, and the frequency components are all diffracted in the same direction. A mirror reflects the light back off the two gratings, and the individual frequencies are recombined into a single beam.

The path length $L(\omega)$ that light takes through the compressor is given by [6]

$$L(\omega) = \frac{b}{\cos\beta'}\left[1 + \cos(\beta + \beta')\right] \tag{4.6}$$

The total phase ϕ acquired by light passing through the compressor is

$$\phi(\omega) = \frac{\omega}{c}L(\omega) - 2\pi\frac{b}{d}\tan\beta' \tag{4.7}$$

where the second term is due to a phase of 2π caused by each ruling of the second grating [6, 30]. This phase can be differentiated twice to give

$$\frac{d^2\phi}{d\omega^2} = -\frac{4\pi^2 bc}{\omega^3 d^2\cos^3\beta'} \tag{4.8}$$

Thus the grating compressor adds negative GVD to a laser pulse travelling through it. The grating stretcher acts on the same principle as the compressor, however a 1:1 telescope is placed between the two gratings. This telescope inverts the sign of the dispersion, and hence pulses travelling through the stretcher are positively chirped. The curved mirrors in Figure 4.4 form this telescope. Mirrors are used as opposed to lenses so no extra dispersion is added by the lens material. The relevant parameter b is not the distance between the two gratings, but the distance between the second grating and the virtual image formed behind the second grating.

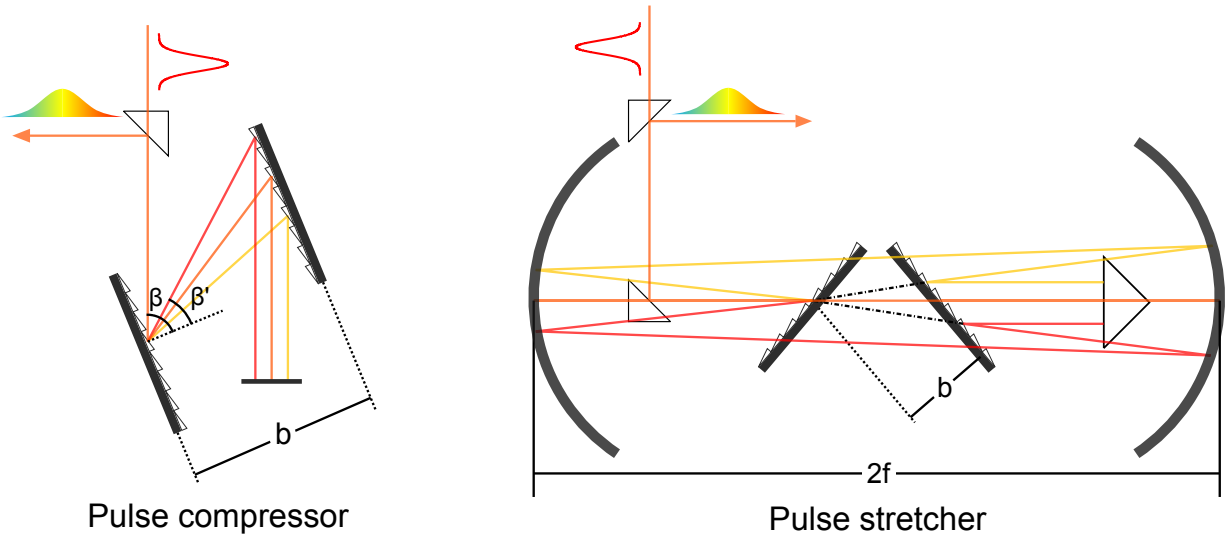

Figure 4.4: Grating-based compressor and stretcher. The compressor consists of two parallel gratings. An input pulse is incident on the first grating at an angle β from normal incidence, and is diffracted by the frequency-dependent angle β', given by (1.23). The light is collimated on the second grating, then back-reflected at a mirror. The returning pulse is at a slightly different height than the incoming light, and is picked off by a mirror. Red-shifted frequencies take an overall shorter path through the compressor than blue-shifted frequencies, creating an antichirped pulse. The separation b of the gratings determines the magnitude of the applied dispersion. The pulse stretcher works on the same principle as the compressor except a 1:1 telescope is placed between the two gratings, inverting the sign of the dispersion and creating a chirped pulse. Two curved mirrors with focal length f are placed a distance $2f$ apart to form this telescope.

The third-derivative of the phase applied by the compressor is given by

$$\frac{d^3\phi}{d\omega^3} = -\frac{3}{\omega}\left(1 + \frac{\frac{\lambda}{d}\left(\frac{\lambda}{d} - \sin\beta\right)}{1 - \left(\frac{\lambda}{d} - \sin\beta\right)}\right)\frac{d^2\phi}{d\omega^2} \tag{4.9}$$

where $\lambda = 2\pi c/\omega$. To determine the relative importance of the third-order term of the expansion of $\phi(\omega)$, it is compared to the second-order term at frequencies near the edge of the pulse bandwidth by the ratio [6]

$$R = \left|\frac{b_3(\omega - \omega_0)^3}{b_2(\omega - \omega_0)^2}\right| \approx \frac{\sigma}{\omega}\left(1 + \frac{\frac{\lambda}{d}\left(\frac{\lambda}{d} - \sin\beta\right)}{1 - \left(\frac{\lambda}{d} - \sin\beta\right)}\right) \tag{4.10}$$

where σ is the bandwidth of the pulse, and the coefficients b_1 and b_2 are defined in (1.11). Grating-based strecher and compressor pairs were used to linearly chirp pulses in the first implementations of CPI [13, 14, 15], and they worked well for these experiments. However these experiments used laser pulses with bandwidth on the order of 10 nm, and hence the third-order term was insignificant compared to the second-order term. With the larger bandwidth of the laser used in the experiments in this thesis, however, the third-order dispersion from these grating-based elements becomes significant, and this has the effect of adding many extraneous features to the CPI signal. There is little freedom in tuning the parameters in (4.10); λ and d are fixed, and it is desirable for σ to be large so the interferometer will have good resolution. The incidence angle β can only be tuned within a very narrow range as the gratings quickly lose efficiency as β deviates from its optimal value.

An optical element known as a *grism* is the combination of a diffraction grating with a prism. A grating is placed adjacent to one face of the prism, and light enters the prism, is diffracted by the grating, and then exits the prism. Grism-based compressors (compressors where the gratings have been replaced with grisms) have been demonstrated to have independently tunable values of second- and third-order dispersion [10, 5]. Compressors and stretchers using grisms are currently being investigated, with the goal of designing systems that add purely quadratic dispersion to a pulse. Hopefully such systems will allow an OCPI system with broadband pulses to be experimentally tested.

Chapter 5

Conclusion

This thesis focused on the dispersion-cancelled imaging technique chirped-pulse interferometery. In Chapter 2 we used this technique to image the internal structure of a biological sample. The required frequency anticorrelations for dispersion cancellation were created by chirping a single light beam with a spatial light modulator in a 4-F system. Chirping the light in this manner produced a signal peak, as opposed to a dip, and allowed all artifacts to be filtered from the signal.

In Chapter 3 pulses were chirped with a nonlinear function before entering the interferometer. It was straightforward to apply the phase for this nonlinear chirp by using the spatial light modulator. Experimentally, applying the nonlinear chirp improved the interferometer resolution by only about half of the expected amount, and it was shown that nonlinearly-chirped pulses cancel dispersion as effectively as linearly-chirped ones. A next step for this experiment would be to use a spatial light modulator with a finer resolution. This would allow the chirping phase to be applied more accurately, and could lead to better system resolution.

Chapter 4 contains a proposal for an experiment to spectrally separate the narrowband component of the background in a chirped-pulse interferometer from the signal. A calculation and a simulation were performed which suggest that the proposed technique could still produce a dispersion-cancelled signal from which artifacts could be filtered. To produce linearly-chirped pulses, grating-based pulse compressors and stretchers were first

investigated. While these grating-based dispersers work well for narrowband pulses, the amount of third-order dispersion they introduce becomes signficant for broadband light. Grism-based dispersers are currently being investigated, which allow the applied second- and third-order dispersion to be tuned independently of each other, unlike grating-based set-ups.

APPENDICES

Appendix A

Measurement of unbalanced interferometer dispersion

While one of the main appeals of CPI is that it produces a dispersion-cancelled signal, a CPI system will operate best if there is no extraneous unbalanced quadratic dispersion in the set-up. Since the amount of dispersion which can be cancelled is limited by the amount the pulses are stretched, it is beneficial to have a way to measure the unbalanced dispersion present in the set-up in order to minimize it.

Consider a CPI set-up where the pulses are chirped by an SLM in a 4f-system (Figure 2.1) with phase $\phi_{chirp} = A(\omega - \omega_c)|\omega - \omega_c|$. Pulses chirped with this phase have an average frequency ω_c, i.e., any given point along the superposition contains the two frequencies $\omega_c \pm \Delta\omega$. The sample arm of the interferometer contains a dispersive element of length L with a wavevector $k(\omega)$. The wavevector for frequencies near the center frequency ω_c is

$$k_{\omega_c}(\omega) \approx k|_{\omega_c} + \left.\frac{dk}{d\omega}\right|_{\omega_c} (\omega - \omega_c) + \frac{1}{2}\left.\frac{d^2k}{d\omega^2}\right|_{\omega_c} (\omega - \omega_c)^2 \tag{A.1}$$

$$= k_{\omega_c} + \alpha_{\omega_c}(\omega - \omega_c)^2 + \beta_{\omega_c}(\omega - \omega_c)^2 \tag{A.2}$$

Light at frequency ω_c will experience a time-delay of $\tau_{\omega_c} = 2\alpha_{\omega_c}L$ as it travels through the

sample arm of this interferometer, where the factor of 2 is due to the double-pass of the dispersive element. Similarly, moving the retroreflector a distance L_{ref} delays the light in the reference arm by $\tau_{ref} = 2L_{ref}/c$. The CPI signal is observed when the interferometer path lengths are balanced for the center frequency ω_c, or when $\alpha_{\omega_c} L = L_{ref}/c$. This equation can be rearranged and differentiated as shown below:

$$L_{ref} = cL\alpha_{\omega_c} \tag{A.3}$$

$$\implies dL_{ref} = cL\frac{d\alpha}{d\omega_c}d\omega_c = 2cL\beta_{\omega_c} \tag{A.4}$$

If the center frequency ω_c of the input light is varied, a plot of the motor position versus the center frequency will have a slope of $2cL\beta_{\omega_c}$. If a CPI system is used to image a dispersion-less sample (such as a mirror) this method can be used to measure the amount of unbalanced quadratic dispersion present in the set-up.

To test this method, the quadratic dispersion introduced by a 6-mm piece of BK7 glass was measured. The position of the CPI peak as a function of the center chirp frequency was measured twice, once with the BK7 inserted and once with it removed. The center-chirp wavelength was varied from 794 nm to 820 nm by changing the chirping function in the SLM. A plot of the difference in the measured peak-positions gives the dispersion introduced by the glass and this is shown in Figure A.1. The delays measured both with and without the BK7 are plotted as well. Each line was fit with a linear function, and the slope is related to the unbalanced quadratic dispersion in the interferometer at the center frequency, $\omega_0 = 2.34\,\mathrm{fs}^{-1}$, which corresponds to a wavelength of 806 nm. The plot of the delay-differences has a slope of $265 \pm 7\,\mathrm{fs}^2$ which is the amount of quadratic dispersion introduced by a double-pass through the BK7. The thickness of the BK7 was measured with a micrometer to be 6.07 ± 0.01 mm which should have a quadratic dispersion of $266\,\mathrm{fs}^2$, within the error of the measured value. The data taken without the BK7 has a slope of $-84 \pm 5\mathrm{fs}^2$ indicating that, at the time of this experiment, optics in the reference arm introduced $168\,\mathrm{fs}^2$ more quadratic dispersion than the optics in the sample arm.

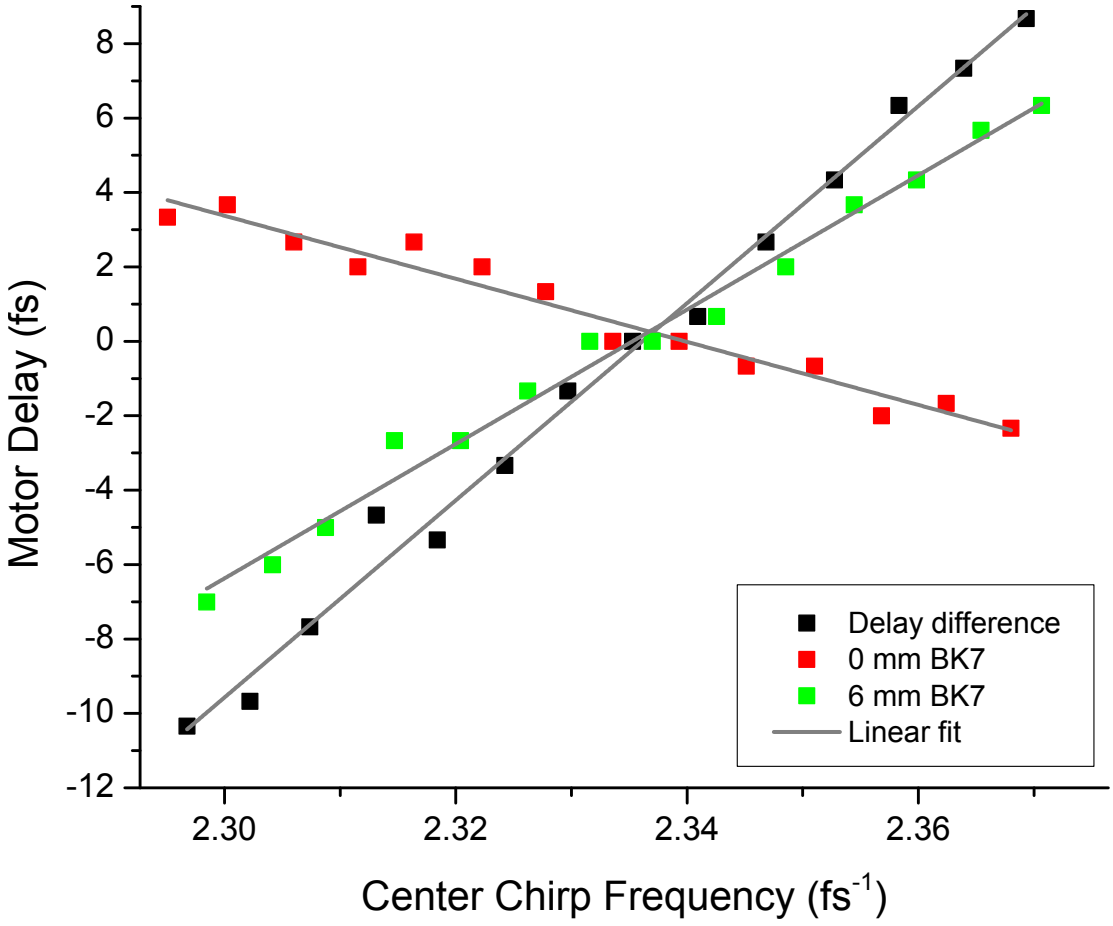

Figure A.1: Measurement of quadratic dispersion from 6 mm of BK7. The CPI peak position (with a constant delay subtracted) is plotted against the center frequency of the chirping function. The red squares are the data taken with a 6-mm thick BK7 optic in the interferometer's sample arm, the green squares are the data with the BK7 removed, and the black squares are the difference between the delays with and without the BK7. The slope of the data taken without the BK7 represents the amount of unbalanced dispersion in the CPI set-up, and the slope of the delay difference represents the amount of quadratic dispersion introduced by the BK7 element.

Appendix B

Griffin-10 alignment technique

The laser used for the experiments in this thesis was the Griffin-10 Ti:Sapphire laser, built by KM-Labs. Occasionally the laser has to be completely realigned. The most difficult part of the realignment is to initiate continuous-wave (CW) lasing, which must be done before the laser can be aligned for modelocking. Here I've reproduced a list of steps for aligning the laser for CW lasing, after the pump beam has been aligned. The technique for aligning the pump beam can be found on page 25 of the Griffin-10 Ti:Sapphire Laser Instruction Manual, which can always be found near the laser. The manual contains a list of steps to align the laser for CW lasing, and I have reproduced steps 1-9 and 13-14 here for completeness. The technique I use deviates from the manual instructions in steps 10-12, and I learned this technique after speaking with a technician from KM-Labs. Figure B.1 depicts the set-up of the laser; this figure has been reproduced from the laser instruction manual.

The procedure for aligning the Griffin-10 for CW follows. The list of steps is meant to be read with reference to Figure B.1, as the number designations for the optics in the laser cavity are often referred to.

1. Ensure that the green pump laser is at minimum power.
2. Verify that the green beam is aligned, as indicated in the previous section (page 25 of the laser instruction manual).

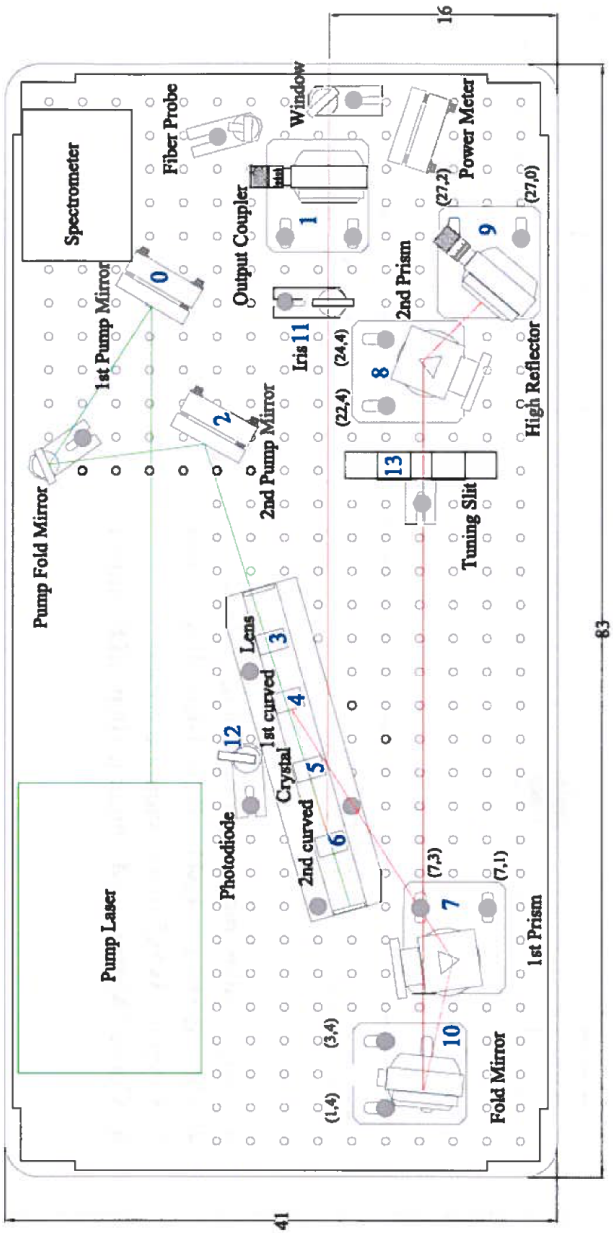

Figure B.1: Layout of KM-Labs Griffin-10 Ti:Sapphire laser. This figure has been reproduced from the KM-Labs Griffin-10 Ti:Sapphire Laser Instruction Manual.

3. Remove the alignment tool from before the lens and open the iris aperture (11) in front of the output coupler.

4. Check that the IR fluorescence spot reflected off of mirror (4) is intercepted by the first prism (7), the fold mirror (10), the second prism (8), and the end high reflector (9). Because the wavelengths are spread out at the second prism (8) and the laser typically operates in the near IR, only a small portion of the visible fluorescence spot will be intercepted by the second prism.

5. Check that the co-propagating IR fluorescence and green beam are incident upon the ouput coupler (1).

6. Ensure that there is a beam block behind the second curved mirror (11).

7. Turn up the green pump power to 5 watts. "Over-pumping" will make it easier to initiate lasing; but once you achieve lasing, turn the pump power down to ∼4.5 W.

8. You should notice where the pump beam passes through the crystal by observing the bright red fluorescence path.

9. You should observe red fluorescence reflected from the second curved mirror (6) focuses ∼10 cm past the output coupler (1) outside the Griffin-10 box. Also, fluorescence from the first curved mirror (4) focuses to a horizontal line at the position of the "far" prism (8).

10. Adjust curved mirrors to ensure the beam is level. Adjust first curved mirror (4) so the beam is 59 mm high before the prism arm mirror (10). Adjust the second curved mirror (6) to make the beam height 59 mm in front of the output coupler.

11. (a) Move the second curved mirror (6) to the CW position (micrometer reading of 5.50 mm). At this point the crystal (5) and the lens (3) probably don't need to be moved. Check the back-reflection from the output coupler (1). Two spots should be observed on a card placed before the second prism (8). One spot is large with ∼1 cm diameter and the other is small. Center the small spot (which is the reflection from the output coupler (1)) in the large spot (which is the

reflection from the first curved mirror (4). It is important to ensure that the heights of the two spots are the same.

(b) The two prisms should be moved further in than for their modelocking positions. ∼80% of the large spot should pass through the first prism (7), and ∼50% of the visible focused line should pass through the second prism (8).

12. Intentionally misalign the retro-reflection from mirror (9) horizontally, then, using an index card, align it vertically with the incoming spot. Next, align the retro-reflection horizontally. Alternately adjust the retro-reflection off mirrors (1) and (9) until lasing is acheived.

13. Optimize the power and mode by alternately tweaking the hoizontal and vertical tilt on both end mirrors (1 and 9) and then adjust the translation micrometers for the lens, second curved mirror (6), and the crystal.

14. Repeat the optimization of each of these components, in a cyclic process, several times.

After the laser has been optimized for CW operation, it can be aligned for mode-locked (i.e., pulsed) operation by following the steps beginning on page 28 of the laser instruction manual.

References

[1] Ayman F. Abouraddy, Magued B. Nasr, Bahaa E. A. Saleh, Alexander V. Sergienko, and Malvin C. Teich. Quantum-optical coherence tomography with dispersion cancellation. *Phys. Rev. A*, 65:053817, May 2002.

[2] J. Altepeter, E. Jeffrey, and P. Kwiat. Phase-compensated ultra-bright source of entangled photons. *Opt. Express*, 13(22):8951–8959, Oct 2005.

[3] Konrad Banaszek, Aleksandr S. Radunsky, and Ian A. Walmsley. Blind dispersion compensation for optical coherence tomography. *Optics Communications*, 269(1):152 – 155, 2007.

[4] Robert W. Boyd. *Nonlinear Optics, Third Edition*. Academic Press, 3rd edition, 2008.

[5] Vikrant Chauhan, Pamela Bowlan, Jacob Cohen, and Rick Trebino. Single-diffraction-grating and grism pulse compressors. *J. Opt. Soc. Am. B*, 27(4):619–624, Apr 2010.

[6] J.C. Diels and W. Rudolph. *Ultrashort Laser Pulse Phenomena*. Optics and photonics. Elsevier Science, 2006.

[7] Baris I. Erkmen and Jeffrey H. Shapiro. Phase-conjugate optical coherence tomography. *Phys. Rev. A*, 74:041601, Oct 2006.

[8] A. Fedrizzi, R. Ursin, T. Herbst, M. Nespoli, R. Prevedel, T. Scheidl, F. Tiefenbacher, T. Jennewein, and A. Zeilinger. High-fidelity transmission of entanglement over a high-loss free-space channel. *Nature Phys.*, 5:389–392, 2009.

[9] A. F. Fercher, W. Drexler, C. K. Hitzenberger, and T. Lasser.

[10] Emily A. Gibson, David M. Gaudiosi, Henry C. Kapteyn, Ralph Jimenez, Steve Kane, Rachel Huff, Charles Durfee, and Jeff Squier. Efficient reflection grisms for pulse compression and dispersion compensation of femtosecond pulses. *Opt. Lett.*, 31(22):3363–3365, Nov 2006.

[11] Julien Le Gouët, Dheera Venkatraman, Franco N. C. Wong, and Jeffrey H. Shapiro. Experimental realization of phase-conjugate optical coherence tomography. *Opt. Lett.*, 35(7):1001–1003, Apr 2010.

[12] C. K. Hong, Z. Y. Ou, and L. Mandel. Measurement of subpicosecond time intervals between two photons by interference. *Phys. Rev. Lett.*, 59:2044–2046, Nov 1987.

[13] R. Kaltenbaek, J. Lavoie, D. N. Biggerstaff, and K. J. Resch. Quantum-inspired interferometry with chirped laser pulses. *Nature Phys.*, 4:864–868, 2008.

[14] R. Kaltenbaek, J. Lavoie, and K. J. Resch. Classical analogues of two-photon quantum interference. *Phys. Rev. Lett.*, 102:243601, Jun 2009.

[15] J. Lavoie, R. Kaltenbaek, and K. J. Resch. Quantum-optical coherence tomography with classical light. *Opt. Express*, 17(5):3818–3825, Mar 2009.

[16] F.L. Lgar, J.M. Fraser, D.M. Villeneuve, and P.B. Corkum. Adaptive compression of intense 250-nm-bandwidth laser pulses. *Applied Physics B*, 74(1):s279–s282, 2002.

[17] O.E. Martinez. Matrix formalism for pulse compressors. *Quantum Electronics, IEEE Journal of*, 24(12):2530–2536, 1988.

[18] Magued B. Nasr, Silvia Carrasco, Bahaa E. A. Saleh, Alexander V. Sergienko, Malvin C. Teich, Juan P. Torres, Lluis Torner, David S. Hum, and Martin M. Fejer. Ultrabroadband biphotons generated via chirped quasi-phase-matched optical parametric down-conversion. *Phys. Rev. Lett.*, 100:183601, May 2008.

[19] Magued B. Nasr, Darryl P. Goode, Nam Nguyen, Guoxin Rong, Linglu Yang, Bjrn M. Reinhard, Bahaa E.A. Saleh, and Malvin C. Teich. Quantum optical coherence tomography of a biological sample. *Optics Communications*, 282(6):1154 – 1159, 2009.

[20] Magued B. Nasr, Bahaa E. A. Saleh, Alexander V. Sergienko, and Malvin C. Teich. Demonstration of dispersion-canceled quantum-optical coherence tomography. *Phys. Rev. Lett.*, 91:083601, Aug 2003.

[21] Avi Pe'er, Yaron Bromberg, Barak Dayan, Yaron Silberberg, and Asher A. Friesem. Broadband sum-frequency generation as an efficient two-photon detector for optical tomography. *Opt. Express*, 15(14):8760–8769, Jul 2007.

[22] M. Pessot, P. Maine, and G. Mourou. 1000 times expansion/compression of optical pulses for chirped pulse amplification. *Optics Communications*, 62(6):419 – 421, 1987.

[23] B. Povazay, K. Bizheva, A. Unterhuber, B. Hermann, H. Sattmann, A. F. Fercher, W. Drexler, A. Apolonski, W. J. Wadsworth, J. C. Knight, P. St. J. Russell, M. Vetterlein, and E. Scherzer. Submicrometer axial resolution optical coherence tomography. *Opt. Lett.*, 27(20):1800–1802, Oct 2002.

[24] K. J. Resch, R. Kaltenbaek, J. Lavoie, and D. N. Biggerstaff. Chirped-pulse interferometry with finite frequency correlations. *Proc. of SPIE*, 7465, 2009.

[25] K. J. Resch, P. Puvanathasan, J. S. Lundeen, M. W. Mitchell, and K. Bizheva. Classical dispersion-cancellation interferometry. *Opt. Express*, 15(14):8797–8804, Jul 2007.

[26] K. M. Schreiter. Optical pulse shaping for chirped pulse interferometry and bioimaging, 2011.

[27] A. M. Steinberg, P. G. Kwiat, and R. Y. Chiao. Dispersion cancellation in a measurement of the single-photon propagation velocity in glass. *Phys. Rev. Lett.*, 68:2421–2424, Apr 1992.

[28] Aephraim M. Steinberg, Paul G. Kwiat, and Raymond Y. Chiao. Dispersion cancellation and high-resolution time measurements in a fourth-order optical interferometer. *Phys. Rev. A*, 45:6659–6665, May 1992.

[29] D. V. Strekalov, T. B. Pittman, and Y. H. Shih. What we can learn about single photons in a two-photon interference experiment. *Phys. Rev. A*, 57:567–570, Jan 1998.

[30] E. Treacy. Optical pulse compression with diffraction gratings. *Quantum Electronics, IEEE Journal of*, 5(9):454–458, 1969.

[31] Paul J. L. Webster, Matthew S. Muller, and James M. Fraser. High speed in situ depth profiling of ultrafast micromachining. *Opt. Express*, 15(23):14967–14972, Nov 2007.

[32] A. M. Weiner. Femtosecond pulse shaping using spatial light modulators. *Rev. Sci. Instrum.*, 71, 2000.

[33] A. M. Zysk, F. T. Nguyen, A. L. Oldenburg, D. L. Marks, and S. A. Boppart.